



Università degli studi di Padova Leibniz Universität Hannover

Dipartimento di Ingegneria Industriale
Corso di laurea magistrale in ingegneria dell'energia elettrica

Numerical simulation and investigation of induction preheating for welding

Author

Gianluca Neridetti [1159850]

Supervisors

Pf. Dr. Ing. Egbert Baake

Ing. Michele Forzan

Dr. Ing. Aleksander Nikanorov

Anno Accademico 2019 – 2020

Abstract

In this thesis an induction heating process for preheating a body before welding is analysed, investigating the feasibility of integration of these two processes. The workpiece subjected to the analysis is made of carbon steel (C45). Often these high strength steels require to be preheated up to a certain temperature in order to reduce the risk of delayed cracking. In particular, the analysed workpiece is a two-part cylindrical body already paired and ready to be weld. These mechanical conditions led to the adoption of a particular inductor design allowing to treat in the proper way the *Heat Affected Zone (HAZ)*; thus a C-shaped inductor has been chosen. Due to the axial symmetry of the inductor-load system, a 2D model has been used to carry out the numerical analysis. The employment of such a model allowing to study the problem in a simple way considering, however, that the power involved in the 2D model is half of the real one. The final temperature distribution must present a good uniformity and the temperature must overcome 300°C. The maximum temperature, besides, must not exceed too much the value of 400°C. The analysis was carried out using software which employs the Finite Element Method (FEM) to evaluate a coupled electromagnetic-thermal analysis. The software used in this study is ANSYS ©. Several models have been implemented considering also the strong non-linear behaviour presented by steel properties with temperature. Moreover, the dependence of magnetic permeability with magnetic field strength was taken into account. To obtain more uniform temperature profiles and to reduce process parameters as heating time and energy consumption, a pair of power control approaches was implemented. Although investigating with constant current leads to good temperature distribution but involving long heating time, the results obtained adopting the power controls result better. Adopting the Pulse power method yields to the halving of the heating time and energy saving is of almost 20%. Additionally, using the accelerated heating approach permits to decrease even more the heating time yielding to a saving of energy of more than 25%. Thus, employing power controls heads to better results although both the computational costs and installation complexity increase.

Sommario

Lo scopo di questa tesi è quello di investigare ed analizzare la fattibilità dell'integrazione di un trattamento elettro-termico, basato sull'induzione elettromagnetica, in un processo di saldatura. L'analisi è stata perseguita con l'ausilio di un software che utilizza il metodo agli elementi finiti (FEM) per risolvere complessi problemi, in cui un'analisi elettromagnetica e termica combinata è richiesta. Il pezzo soggetto all'analisi è un composto in acciaio C45, materiale che si presta bene per impieghi quali la costruzione di organi meccanici duri e tenaci. Spesso gli acciai con medio o alto contenuto di carbonio richiedono un trattamento di preriscaldamento nella zona di saldature. Ciò fa sì che si riduca al minimo il rischio di formazione di microcricche al loro interno. In particolare, il pezzo meccanico in analisi è composto da due parti cilindriche accoppiate e pronte per essere saldate tra loro. L'impossibilità nell'accoppiare a tale carico un induttore a singola o multi spira, ha fatto propendere per la scelta di utilizzare un induttore a forma di C. Grazie alla simmetria assiale del sistema carico-induttore è stato possibile condurre un'analisi numerica sul corrispondente modello 2D, tenendo però in considerazione che tale modello non descrive perfettamente il sistema reale. Sono state quindi condotte diverse investigazioni e al termine è stato applicato un coefficiente correttivo, tenente conto che la potenza del modello 2D è metà di quella impiegata nel sistema reale. Tramite le simulazioni si sono valutati i parametri geometrici ed elettrici del sistema che permettono di ottenere una distribuzione di temperatura uniforme in tutto lo spessore della HAZ. I valori di temperatura nella regione trattata, inoltre, devono mantenersi in un intervallo che va dai 300°C ai 400°C così da ottenere un trattamento efficace. I modelli implementati tengono conto della forte dipendenza non lineare che hanno le caratteristiche dell'acciaio al variare della temperatura. Inoltre è stato implementato un algoritmo che simula la dipendenza della permeabilità magnetica con l'intensità del campo magnetico, rendendo il modello più prossimo alla realtà. Dopo aver condotto diverse analisi, sono stati implementati due controlli di potenza; essi hanno evidenziato che, modulando la potenza fornita al sistema, si ottiene un risparmio in termini di tempo e di consumo di energia. Adottando una modulazione di potenza ad impulsi si ottiene un dimezzamento del tempo di processo e un risparmio di energia

di quasi il 20%. Una ulteriore diminuzione del tempo di trattamento si ottiene implementando una modulazione di potenza secondo il metodo di riscaldamento accelerato. Questo approccio porta ad un risparmio di energia di poco superiore al 25%, rispetto all'energia utilizzata senza alcun tipo di controllo sulla potenza. Sebbene l'impiego di tecnologie basate sull'induzione integrate nei processi di saldatura sia ancora poco diffuso nel settore manifatturiero, la versatilità, l'assenza di produzione ed utilizzo di sostanze inquinanti e la riduzione di rumore nei siti di installazione rende queste tecnologie idonee per sostenere la transizione energetica industriale verso una sempre più diffusa elettrificazione dei processi produttivi.

Contents

Abstract	iii
1 Introduction	1
1.1 About welding processes	1
1.2 Aim of the research	2
1.3 Approach to the ananalysis	4
2 Theoretical background	5
2.1 About induction heating	5
2.1.1 Principles	5
2.1.2 Overview of processes and systems	8
2.2 Heating of a cylindrical body	9
2.2.1 Induced Current and Power density distributions	10
2.2.2 Induced power and equivalent impedance of the system	16
2.2.3 Heating of hollow workpieces	20
2.3 Electrical parameters	24
2.3.1 Resistance and reactance of inductor	24
2.3.2 Electrical efficiency	27
2.3.3 Power and Quality factor	28
2.3.4 Thermal transient analysis	30
2.4 Variations of material features	36
3 Numerical approach	43
3.1 <i>FEA</i> : Finite Element Analysis	43
3.1.1 Electromagnetic and thermal physics characterization	43
3.1.2 Solving PDEs	47
3.2 Ansys Parametric Design Language (APDL)	49
3.2.1 The Preprocessing stage	54
3.3 Strategy of investigation	59
3.3.1 Parameters determination	60

3.4	Case study 1	63
3.5	Case study 2	66
3.6	Case study 3	68
3.7	Case study 4	70
3.8	Case study 5	72
4	Summary of results	75
	Bibliography	84

Chapter 1

Introduction

In this starting chapter the welding process and all its issues and characteristics are presented. As one of the most critical and quality-related industrial process, a good weld has to be guaranteed in any conditions and for any workpiece.

1.1 About welding processes

Welding processes are fabrication or sculptural processes which realise a permanent joint of two workpieces, usually metals or thermoplastics, by means of localized heat to melt the parts together and allowing them to cool causing fusion. In addition, to melting the base metal, a filler material is usually added to the joint to form a pool of molten material (the weld pool) that cools to form a joint that, based on weld configuration, can be stronger than the base material. Many different energy sources can be used for welding, including a gas flame (chemical), an electric arc (electrical), a laser, an electron beam, friction, and ultrasound. Welding is a hazardous process and precautions are required to avoid burns, electric shock, vision damage, inhalation of poisonous gases and fumes, and exposure to intense ultraviolet radiation. Due to its huge impact on the integrity, reliability and security of mechanical elements, weld quality is a crucial factor and has to be guaranteed.



Figure 1.1: The cross-section of a welded butt joint. The darkest grey represents the weld, the medium grey the *heat-affected zone* and the lightest grey the base material.

The most critical region of a welded workpiece is the so-called *HAZ (Heat-Affected Zone)*. In theory, the *HAZ* includes all regions heated to any temperature above the ambient. From a practical point of view, however, it comprises only those regions

that are measurably influenced by the heat of the welding process. [1] Due to the heating experienced within the *HAZ*, the microstructure and properties in this region change. Even the *HAZ* could vary in size and strength, depending on the used material and the heat source, these changes are usually undesirable and lead to this zone becoming weaker than the base material. Steels, for instance, usually required to be preheated, prior to welding, in order to reduce the risk of cracking. This detrimental phenomena, often referred to as *delayed cracking*, occurs after the weld has cooled to ambient temperature, which may be several hours after welding. The steels most susceptible to this type of cracking are those that transform to martensite during the cooling portion of the process. Moreover, delayed cracking is associated with dissolved hydrogen that remains into the weld metal during solidification and transformation to martensite. In order to minimize the risk of its occurrence, usually, the base material is preheated to slow the cooling rate. The use of preheating prevents the formation of crack-susceptible microstructure and promotes the escape of hydrogen from steel by diffusion.[1]

1.2 Aim of the research

In general, the preheating process is made by mean of an open flame from a torch, as it is easy to use offers simple setup and portability. On one hand, this common method has a low initial investment cost and it's well known by almost any welder. On the other hand, preheating with an open flame may be inefficient compared to other solution because much of the heat is lost into the surrounding environment. It yields insufficient temperature homogeneity throughout the treated zone, affecting the weld quality. Flame preheating also give rise to safety hazards and has special storage requirements for explosive gases, usually propylene and propane.

Table 1.1: Chemical composition of steel C45

Element	C %	Si %	Mn %	P %	S %	Cr %	Mo %	Ni %
MIN	0.42	-	0.50	-	0.020	-	-	-
MAX	0.45	0.40	0.80	0.030	0.035	0.40	0.10	0.40

Because these gases are composed of carbon and hydrogen, they can contribute to increasing the risk of delayed cracking. Due to the inefficiency of this method other options such as oven furnaces, used for preheating especially small parts, and induction heating can be used. The latter permits to cut out almost all the withdraws of using a torch, leading to a higher quality process.

In this study, a workpiece made of *steel C45* has been considered. The C45 is a medium carbon steel used for mechanical engineering components with chemical

composition as listed in Table 1.1. This metal requires to be preheated before welding although its good mechanical properties and weldability. The main aim is to study the feasibility of preheating a thick cylindrical workpiece by the adoption of an induction heating system and gain a good, and uniform, temperature profile throughout the *HAZ*. It has to be heated up to a temperature above the martensite initial temperature M_s in order to reduce the rate at which the metal cools down from the welding temperature and avoid the transformation from austenite to martensite. In Fig. 1.2 the *Time Temperature Transition Diagram* shows the required holding time, temperature and the cooling rates for the specific heat treatment of steel C45. Observing the diagram is immediate to estimate in which temperature range M_s is ($325\text{ }^\circ\text{C}$ [2]). As a result of that, for the investigation a preheat temperature T_{PH} varying from 300 to $400\text{ }^\circ\text{C}$ will be considered valid, with the higher value referred to the surface temperature.

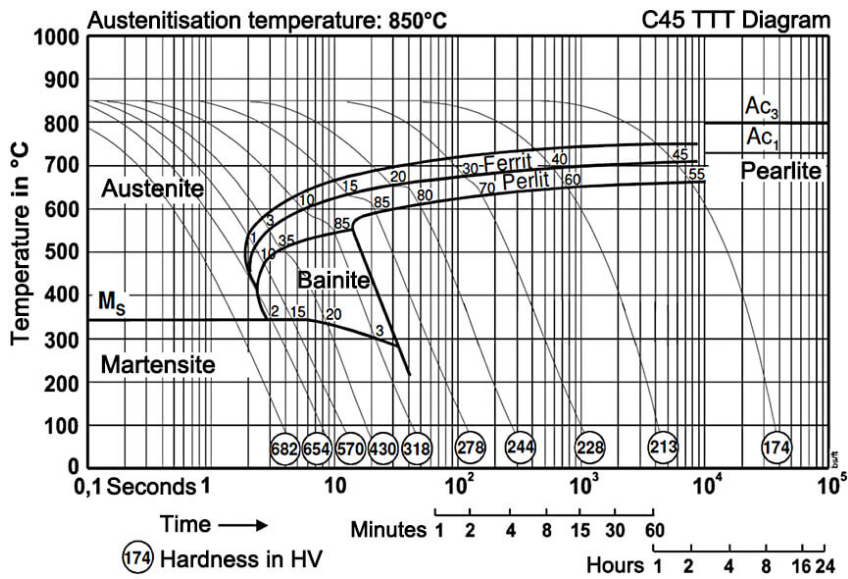


Figure 1.2: Time Temperature Transition Diagram of Steel C45

Induction heating is well-known and practically used for heat treatments in pipe fabrication and welding. Although this is the larger area of application, this method is a flexible option that can be tailored to part size and geometry. A further benefit of induction systems is that they offer fast time to temperature. It's possible to achieve the result in minutes compared to hours for resistance heating, especially on thick parts.

1.3 Approach to the analysis

The study pertains to the electrical and thermal analysis, i.e. to design an inductor capable of satisfying a defined temperature profile. The design of an inductor takes into account a large number of variable and parameters on which the designer can act. The electrical variables such as the frequency, as well as the electrical power and current, influence mainly the temperature radial distribution whereas the inductor geometry is important to differentiate the temperature in the axial direction. Furthermore, the inductor design is forced by both material's typology and shape. In this case, the workpiece is a two-part hollow cylinder of steel C45 (medium carbon steel), paired and ready to be jointed. It has an external diameter that varies between 232 mm and 240,8 mm in the proximity of the weld, causing an irregular thickness of the *HAZ* which is approximately 24,5 mm. A further complication consists of some work constraints that forced to adopt a C-shaped inductor. In other words, the cylinder is mechanically bounded and it's impossible to use a single, or multi, turn coil. Therefore, the idea is to design a linear odd-shaped inductor, as shown in Fig. 1.3 to obtain a thorough heating of the welding zone. In general, an accurate treatment requires that the minimum preheat temperature to be established at a distance that is at least equal to the thickness of the thickest part of the *HAZ*, in all direction from the weld. This extension should be covered as much as possible.



Figure 1.3: Sketches of the inductor-workpiece system (not to scale)

In the following investigation, the numerical analysis is conducted using the commercial *FEM* simulation software ANSYS ©. The simple geometry of the workpiece recommends to implement an axisymmetric 2D model to lessen the computational cost. However, using the two dimensional model leads to study the inductor as a single turn coil. That brings to further consideration on the flowing current values, since the energy do not change considering the workpiece keeps in rotation heated up by a single or a half turn coil. Thus, the current in the 2D model is $\sqrt{2}$ time smaller than the real one. Once implement a model that fulfil the requirements, further investigations, based mainly on energy consumption, have been carried out. A few experimental activities would had been necessary to validate the investigation but unfortunately, it was not possible to carry them out.

Chapter 2

Theoretical background

In this chapter are presented the main strengths of induction heating processes. The principle quantities are analysed with a theoretical approach but, in order to obtain them, simplifying hypothesis are adopted.

2.1 About induction heating

The discovery of the underlying principles of electromagnetic induction is credited to the English scientist Michael Faraday in 1831. At first, he emphasized the negative effect of the phenomenon, and huge effort was put toward the research of alternative methods that would reduce these negative effect. The study of this subject was mainly based on making transformers, motors and generators more efficient. By the early 20th century, the iron and steel industry led the development of devices based on induction for metal melting. Nowadays, induction heating is one of the most spread solution for heating electrically conductive items, mostly metallic materials. This technology is diffused in the manufacturing industry thanks to its several suitable features. Among all, the generation of heat directly inside the object itself. Summing up all the features, induction heating is characterized by a rational use of electric energy, high power density and good efficiency.

2.1.1 Principles

Induction heating uses the heat produced by currents induced within a conducting body concatenated by an alternating magnetic field. The magnetic flux is generated by the flow of an alternating current in the inductor, in turn, arises by an applied alternating voltage. This current will create, in the surrounding of the coil, a time-varying magnetic field that has a frequency equal to the one of the applied voltage.

The magnetic field is so responsible for the induction of eddy currents within the target object. Thus, without a direct contact between elements, the heat source is set into the workpiece. Usually, the load is placed in front of the inductor coil or encircled by it, as in Fig. 2.1.

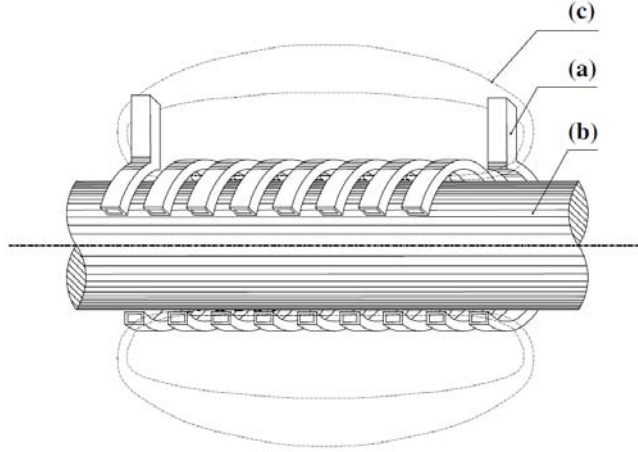


Figure 2.1: Typical arrangement of induction coil (a) and load (b) and distribution of magnetic field lines (c) [3].

The current's distribution in both load and inductor is not uniform because of electromagnetic phenomena, including *skin*, *ring* and *proximity* effect.

Skin effect A conductor supplied with DC current, the current density is uniform throughout all the cross section. However, an alternating current flow produces a decrease of the current density from the surface towards the core of the body. Given a cylindrical conductor, the variation can be described with a decreasing exponential trend. The current density is so condensed upon the *skin* of the conductor, within a layer of thickness called *penetration depth*, defined as:

$$\delta = \sqrt{\frac{\rho}{\mu\pi f}} \quad (m). \quad (2.1)$$

It's caused by the alternating magnetic field generated by the flowing alternating current. The variation in time of this generated magnetic field, in turn induces currents, as shown in Fig. 2.2, which are additive in the outer layer and opposite close to the core. The skin effect brings to an increase of the electric resistance because the effective cross section, occupied by the current, is reduced. From the Eq. (2.1) it is easy to notice that the skin effect is maximized with the increase of the frequency f , minimizing the penetration depth δ .

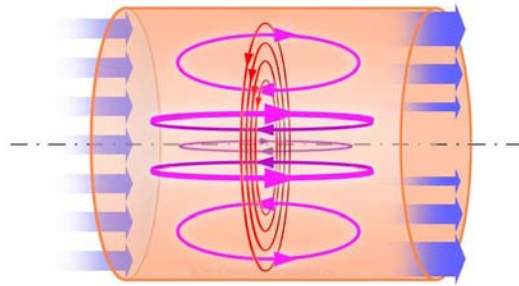


Figure 2.2: Skin effect in a cylindrical conductor

Proximity effect The discussion of the skin effect in a conductor does not consider the presence of other conductors carrying currents in the surrounding area. In most practical application the system presents more than a single conductor. The proximity of two, or more, conductors gives rise to a redistribution of the current density inside them. The divergent direction of the currents fosters an increase of magnetic field in the gap between the conductors. The field lines produced by the first conductor pass through the near one, inducing eddy currents. It results in a concentration of current density on the inside-facing surfaces of the conductors and a reduction on the outward-facing sides. By contrast, if the currents flow in the same direction the magnetic field is more intense in the external volume surrounding the conductors, as shown in Fig. 2.3. This leads to a gathering of currents on the outward-facing surfaces.

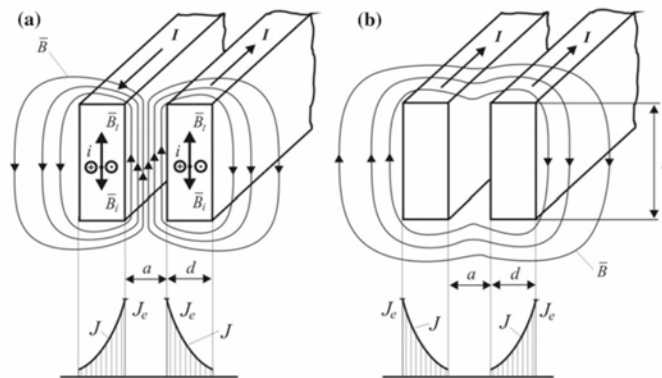


Figure 2.3: Proximity effect [4]

The skin and proximity effects are two manifestation of the same physical principle: a good conductor doesn't permit to a magnetic flux line to penetrate through it. In fact, the flux lines penetrate the conducting body only within a certain depth, as already mentioned before. Considering an ideal insulating body however, the magnetic field penetrates throughout it without any consequence, including skin effect or Joule heat. Comparing these two effects, is good to point out that they

differ from the origin of the magnetic flux. The skin effect is caused by the field generated by the current flowing through, instead the proximity one is triggered by an external magnetic source.

Ring effect This effect shares origin with the aforementioned ones but it takes place when the conductor is bent to form a ring. In this case, magnetic field lines are more dense inside the ring and, as a result, the current density is bigger in the inner layer of the ring.

2.1.2 Overview of processes and systems

Heating processes are suitable for the achievement of different temperature profiles. The choice of a particular process is driven by the type of heat treatment that is aimed to pursue. Superficial heating, for instance, is obtained with hardening processes whilst other situations require the adoption of through heating ones. For a heat treatment prior to welding, the latter kind of process is prescribed.

In general, four basic heating modes can be distinguish: *static*, also known as single shot, *progressive*, *pulse* and *oscillating*. The static heating mode is referred to a process in which neither the workpiece nor the inductor moves linearly. This mode is effectively used for selective hardening in which only a particular part has to be heated up. However, rotation is often added (also in the through heating cases) especially if the load is cylindrical or rotational symmetric. The progressive mode may be used for heating long longitudinal elements such as pipes and tubes, characterized by small diameters. Differently, the pulse heating mode has to do with short bursts of heat which permit to control and maintain a desired temperature profile, specially suitable for through heating processes. It is also feasible for induction hardening of gears, critical components and high carbon steels, that have conspicuous tendency to crack. Lastly, oscillating heating mode exploits a single or multi-coil inductor in which the load moves back and forth. This approach brings to save space but is only used in mass heating processes.

In order to obtain a specific temperature profile, the choice of a worthy heating mode is not sufficient. It has to be followed by a tailor-made design of the inductor (see Fig. 2.4.)

Recalling the fact that the distribution of the induced current depends on the frequency of the exciting magnetic field, depending on the requirements of the application, the coil is fed with a current at industrial (50/60 Hz) or higher frequency, up to some MHz. As a result of that, different types of solid-state components are embedded in the electronic that powers and controls the system, following the requirements on the switching frequency and the voltage and current they must carry.

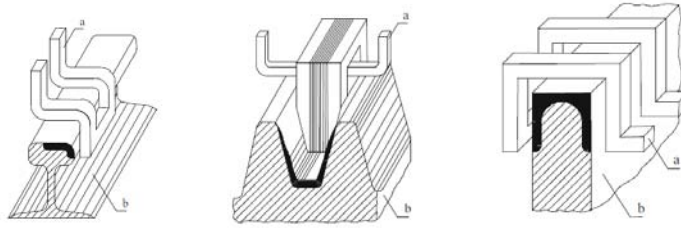


Figure 2.4: Examples of different induction coil-load systems (**a** coil **b** load) [3].

Thus, a converter is one of the main component of a induction installation. It collects the power from the supplying grid, at industrial frequency, and permits to manage the output value of frequency. In short, the applied voltage has to be rectified, through a diode rectifier (AC/DC) and then a second conversion, through an inverter (DC/AC), provides an output voltage at the prescribed frequency. Among all the components of an induction heating system, schematically illustrated in Fig. 2.5, particular importance has the capacitor bank indispensable for the power factor compensation of the system, usually very low.

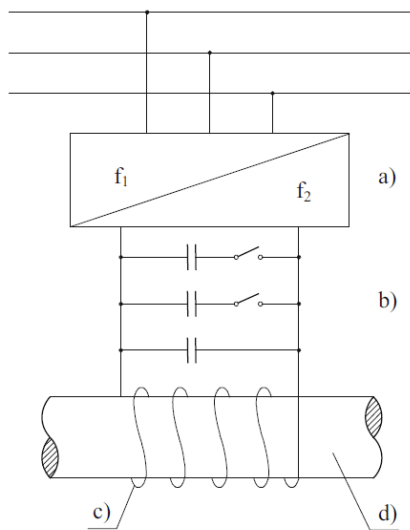


Figure 2.5: Main elements of an iduction heating installation (**a** frequency converter; **b** capacitor bank; **c** inductor coil; **d** body to be heated) [3].

2.2 Heating of a cylindrical body

A solid cylinder with constant electrical resistivity and magnetic permeability, placed inside a coil fed by a sinusoidal current, is consider and illustrated in Fig. 2.6.

With reference to a cylindrical coordinate system (r, φ, z) , the following notation are used [3]:

All these notations will be recursive in the rest of the study with obvious meaning.

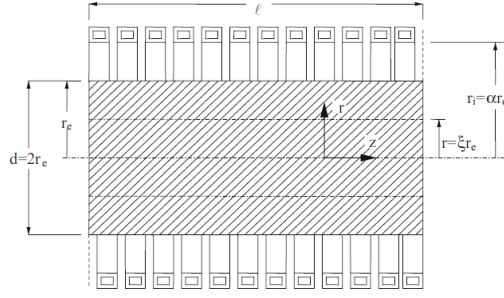


Figure 2.6: Cylindrical inductor-load system

r_e, r_i	External radius of the cylinder and inner radius of the inductor coil [m]
$\xi = \frac{r}{r_e}$	Dimensionless radius ($0 \leq \xi \leq 1$)
$\alpha = \frac{r_i}{r_e}$	$\alpha > 1$
ℓ	Axial length of induction coil and cylinder [m]
N	Number of turns
I	Root mean square value of coil' s current [A]
f	Frequency [Hz]
$\omega = 2\pi f$	Angular frequency, or pulsation, of coil' s current [$\frac{rad}{s}$]
μ_0	Vacuum magnetic permeability ($4\pi \cdot 10^{-7}$ [H/m])
ρ, μ	Electrical resistivity [Ωm] and relative magnetic permeability of the load

2.2.1 Induced Current and Power density distributions

Assuming that the section of length ℓ of the system is a portion of a cylindrical configuration of infinite axial length, the magnetic field between coil and load has a single component directed along z and an intensity defined by:

$$\dot{H}_e = \frac{N \dot{I}}{\ell}$$

which corresponds to the one produced by an empty inductor without load. The dotted letters stand for *sinusoidal quantities* where the generic one $a(t) = \sqrt{2} A \sin(\omega t + \alpha)$ has been written using the *phasor* notation $\dot{A} = A e^{j\alpha}$.

The Maxwell equations:

$$\nabla \cdot \mathbf{D} = \rho_c \quad (2.2a)$$

$$\nabla \cdot \mathbf{B} = 0 \quad (2.2b)$$

$$\nabla \times \mathbf{E} = -\frac{\partial \mathbf{B}}{\partial t} \quad (2.2c)$$

$$\nabla \times \mathbf{H} = -\frac{\partial \mathbf{D}}{\partial t} + \mathbf{G} \quad (2.2d)$$

where ρ_c is the volumetric charge density [C/m^3], \mathbf{D} the electric induction [C/m^2],

\mathbf{E} the electric field [V/m], \mathbf{H} the magnetic field [A/m] and \mathbf{G} the current density [A/m²], and constitutive equation:

$$\begin{aligned}\mathbf{D} &= \varepsilon \varepsilon_0 \mathbf{E} \\ \mathbf{B} &= \mu \mu_0 \mathbf{H} \\ \mathbf{E} &= \rho \mathbf{G}\end{aligned}$$

are the fundamentals of electromagnetism.¹ In this case, given the range of frequencies normally used, the displacement currents are neglected and under the assumptions of sinusoidal wave form and linear behaviour of the material, Maxwell equations can be rewritten from Eq. (2.2) as follows:

$$\begin{cases} \text{rot } \dot{\mathbf{H}} = \frac{\dot{\mathbf{E}}}{\rho} \\ \text{rot } \dot{\mathbf{E}} = -j\omega\mu\mu_0\dot{\mathbf{H}} \end{cases} . \quad (2.4)$$

Under all the hypothesis already done, the current density $\dot{\mathbf{G}}$ and magnetic field $\dot{\mathbf{H}}$ vectors present null components:

$$\begin{cases} \dot{\mathbf{G}}(r) = (0, \dot{G}_\varphi, 0) \\ \dot{\mathbf{H}}(r) = (0, 0, \dot{H}_z) \end{cases}$$

and so that Eq. (2.4) can be written as follows:²

$$\begin{cases} \text{rot}_\varphi \dot{\mathbf{H}} = -\frac{\partial \dot{H}_z}{\partial r} = \frac{\dot{E}_\varphi}{\rho} \\ \text{rot}_z \dot{\mathbf{E}} = \frac{\partial \dot{E}_\varphi}{\partial r} + \frac{\dot{E}_\varphi}{r} = -j\omega\mu_0\mu\dot{H} \end{cases} . \quad (2.5)$$

Therefore, excluding, hereafter, the indexes φ and z it's possible to combine Eq (2.5) and obtain the following equation:

$$\frac{\partial^2 \dot{H}}{\partial r^2} + \frac{1}{r} \frac{\partial \dot{H}}{\partial r} - j \frac{\omega\mu_0\mu\dot{H}}{\rho} = 0 \quad (2.6)$$

This differential equation can be written in function of dimensionless parameters: $\beta^2 = -j \frac{\omega\mu_0\mu}{\rho} r_e^2 = -jm^2$, $m = \frac{\sqrt{2}r_e}{\delta}$ and $\xi = \frac{r}{r_e}$, with δ the penetration depth, previously defined by Eq. (2.1).

¹Bond characters stand for vectorial quantities

²In a cylindrical coordinate system, the **rotor** of a generic vector \mathbf{A} , can worked out as:
 $\text{rot}\mathbf{A} = \left(\frac{1}{r} \frac{\partial A_z}{\partial \varphi} - \frac{\partial A_\varphi}{\partial z}\right) \hat{\mathbf{u}}_r + \left(\frac{\partial A_r}{\partial z} - \frac{\partial A_z}{\partial r}\right) \hat{\mathbf{u}}_\varphi + \left(\frac{1}{r} \frac{\partial(rA_\varphi)}{\partial r} - \frac{\partial A_r}{\partial \varphi}\right) \hat{\mathbf{u}}_z$

It brings to the definition of the *Bessel differential function* or order zero, as follows:

$$\frac{\partial^2 \dot{H}}{\partial \xi^2} + \frac{1}{\xi} \frac{\partial \dot{H}}{\partial \xi} + \beta^2 \dot{H} = 0 \quad . \quad (2.7)$$

The general solution can be written in the form:

$$\dot{H} = \dot{C}_1 \cdot J_0(\sqrt{-jm\xi}) + \dot{C}_2 \cdot Y_0(\sqrt{-jm\xi})$$

or briefly :

$$\dot{H} = \dot{C}_1 \cdot J_0(\beta\xi) + \dot{C}_2 \cdot Y_0(\beta\xi) ,$$

with J_0 and Y_0 are order zero Bessel functions, of first and second kind respectively, of complex argument x , properly illustrated in Fig. 2.7.

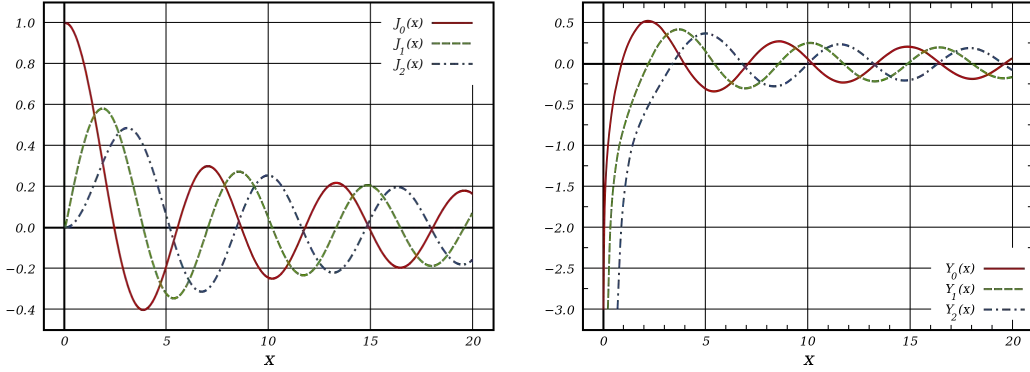


Figure 2.7: Plot of Bessel functions of the first $J_k(x)$ and second kind $Y_k(x)$, for integer orders $k = 0, 1, 2$

The integration constants \dot{C}_1 and \dot{C}_2 can be established with the boundary conditions:

$$\dot{H} \neq \infty \quad \text{for} \quad \xi = 0; \quad \dot{H} = \dot{H}_e \quad \text{for} \quad \xi = 1 .$$

Hence, being $Y_0(0) = -\infty$, we have $\dot{C}_2 = 0$ and $\dot{C}_1 = \dot{H}_e / J_0(\sqrt{-jm})$, from the first and second condition respectively.

Replacing these values in Eq. (2.8), for the amplitude of the vector of magnetic field strength, it gives:

$$\dot{H} = \dot{H}_e \frac{J_0(\sqrt{-jm\xi})}{J_0(\sqrt{-jm})} \quad . \quad (2.9)$$

It may be more practical sometimes evaluate separately real and imaginary parts of $J_0(\sqrt{-ju})$ adopting the relationship:

$$J_0(\sqrt{-ju}) = ber(u) + j beri(u) \quad .$$

Hence, equation (2.9) becomes:

$$\begin{cases} \dot{H} = \dot{H}_e \frac{ber(m\xi) + j bei(m\xi)}{ber(m) + j bei(m)} \\ \left| \frac{\dot{H}}{\dot{H}_e} \right| = \sqrt{\frac{ber^2(m\xi) + bei^2(m\xi)}{ber^2(m) + bei^2(m)}} \end{cases} \quad (2.10)$$

The last equations highlighted the dependence of the complex vector of the magnetic field \dot{H} not only on the dimensionless radius $\xi = r/r_e$, but also on $m = \sqrt{2}r_e/\delta$. Furthermore, they specify that moving from the surface towards the axis of the cylinder (i.e. varying ξ), either the amplitude and the phase angle of the vector change in respect with the values at the outer layer.

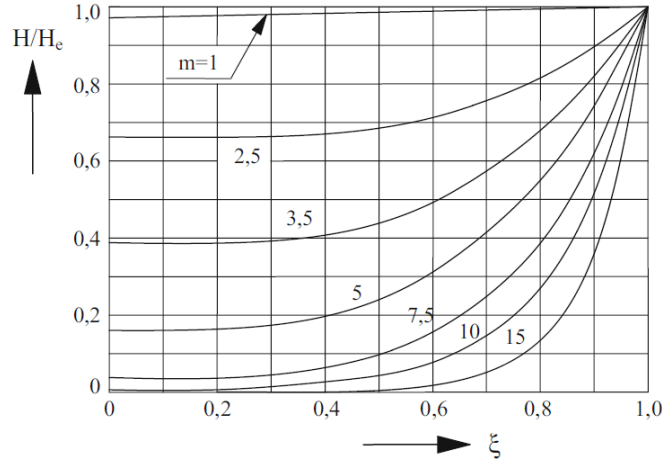


Figure 2.8: Distribution of magnetic field intensity H along the radius, referred to the value H_e at the surface. [3]

The curves in Fig. 2.8 show the repulsive effect of the induced currents on the magnetic field which concentrates in the outer layers. Moreover, higher is the value of m more marked is the phenomenon.

The moduli of electric field \dot{E} and current density \dot{G} vectors are evaluable starting from the first of Eqs. (2.5) and (2.9) respectively. Recalling that is $J'_0(u) = -J_1(u)$ we have:

$$\dot{E} = \sqrt{-j} \cdot \dot{H}_e \cdot \frac{\rho}{\delta} \cdot \sqrt{2} \cdot \frac{J_1(\sqrt{-j}m\xi)}{J_0(\sqrt{-j}m)}, \quad (2.11)$$

$$\dot{G} = \frac{\dot{E}}{\rho} = \sqrt{-j} \cdot \dot{H}_e \cdot \frac{\sqrt{2}}{\delta} \cdot \frac{J_1(\sqrt{-j}m\xi)}{J_0(\sqrt{-j}m)}. \quad (2.12)$$

After having designated the surface values ($\xi = 1$) of electric field and current density

as \dot{E}_e and \dot{G}_e respectively, is possible to carry out the next relationship:

$$\frac{\dot{E}}{\dot{E}_e} = \frac{\dot{G}}{\dot{G}_e} = \frac{J_1(\sqrt{-j}m\xi)}{J_1(\sqrt{-j}m)} \quad (2.13)$$

From Eqs. (2.11) and (2.12), separating real and imaginary parts, the current density distribution can be evaluated by the following formulas:

$$\dot{G} = \frac{\dot{E}}{\rho} = -\frac{\dot{H}_e}{r_e} m \frac{\text{ber}'(m\xi) + j \text{bei}'(m\xi)}{\text{ber}(m) + j \text{bei}(m)} \quad (2.14)$$

$$\begin{cases} \frac{\dot{E}}{\dot{E}_e} = \frac{\dot{G}}{\dot{G}_e} = \frac{\text{ber}'(m\xi) + j \text{bei}'(m\xi)}{\text{ber}'(m) + j \text{bei}'(m)} \rho \\ \left| \frac{\dot{E}}{\dot{E}_e} \right| = \left| \frac{\dot{G}}{\dot{G}_e} \right| = \sqrt{\frac{\text{ber}'^2(m\xi) + j \text{bei}'^2(m\xi)}{\text{ber}'^2(m) + j \text{bei}'^2(m)}} \end{cases} \quad (2.15)$$

In specific, from the Eqs. (2.12) and (2.14) it's possible to write the following relationships for the surface value of the induced current density:

$$\begin{cases} \dot{G}_e = \frac{\dot{E}_e}{\rho} = \sqrt{-j} \dot{H}_e \frac{\sqrt{2}}{\delta} \frac{J_1(\sqrt{-j}m)}{J_0(\sqrt{-j}m)} = -\frac{\dot{E}_e}{r_e} m(P + jQ) \\ \left| \dot{G}_e \right| = \frac{\left| \dot{H}_e \right|}{r_e} m \sqrt{P^2 + Q^2}, \end{cases} \quad (2.16)$$

having established $P + jQ$ as follows:

$$P + jQ = -\sqrt{-j} \frac{J_1(\sqrt{-j}m)}{J_0(\sqrt{-j}m)} = \frac{\text{ber}'m + j \text{bei}'m}{\text{ber}m + j \text{bei}m} \quad (2.17)$$

In particular, P and Q , whose depend only by the m parameter, play a key role in evaluating the power induced in the workpiece. Figure 2.9 shows their trend in function of m , highlighting their convergence to $1/\sqrt{2}$ for $m \rightarrow \infty$.

From the last current density expressions is possible to draw a few conclusions down:

- the induced currents are phase-shifted and are lessen in amplitude moving from the surface towards the axis of the load (see Fig. 2.10);
- on the axis of the cylinder, the current density is always null, and, as the value of m grows, it concentrates in an ever thinner layer beneath the surface;
- keeping r_e and H_e constant, the amplitude of G_e will get bigger with higher values of m , as emphasized in the second of Eqs. (2.16);
- in reality, if the strength of the exciting magnetic field is kept constant, different

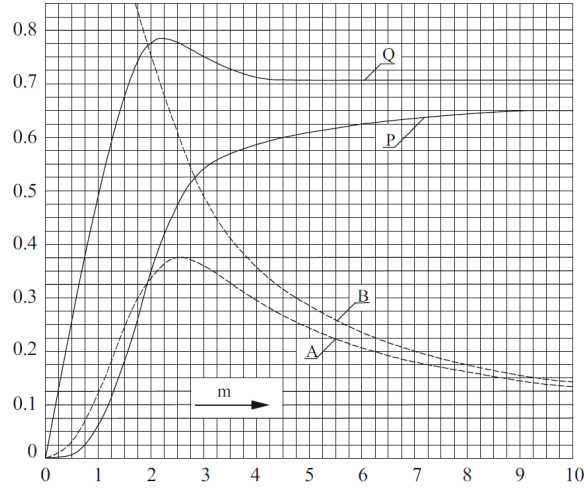


Figure 2.9: Values of the coefficients P and Q . [3]

current density distributions are generated along the radius by the changing of the frequency, as shown in Fig. 2.11;

- from the curves is notable that, the distributions are almost linear at fairly low frequency, as long as, they tend to an exponential at high frequency.

Therefore, the only parameters on which is possible to act in order to adjust the values and distributions of the induced current density are \dot{H}_e and f . Nevertheless, the choice of this parameters isn't arbitrary and numerous other details must be taken into account. In particular, these parameters must fit the process specifics (i.e. temperature profile), the energy transmission efficiency between coil and load, the converter and cooling system costs and the electromagnetic forces acting on inductor and workpiece.

After the relationships of the induced current density, the distributions of the *induced specific power per unit of volume* are immediately derived. Being $w = \rho G^2$ the specific power at a generic radius, and $w_e = \rho G_e^2$ its corresponding value on the surface, we have:

$$\left| \frac{w}{w_e} \right| = \left| \frac{J_1(\sqrt{-j}m\xi)}{J_1(\sqrt{-j}m)} \right|^2 \quad (2.18)$$

$$w_e = \rho \frac{H_e^2}{r_e^2} m^2 (P^2 + Q^2) \quad . \quad (2.19)$$

The above expression and the curves of Fig. 2.12 point out that also the induced power is unevenly distributed inside the load, with a steep slope from the surface to the core, accentuated by the increase of the frequency.

In order to simplify the analysis, the upcoming approximations can be used:

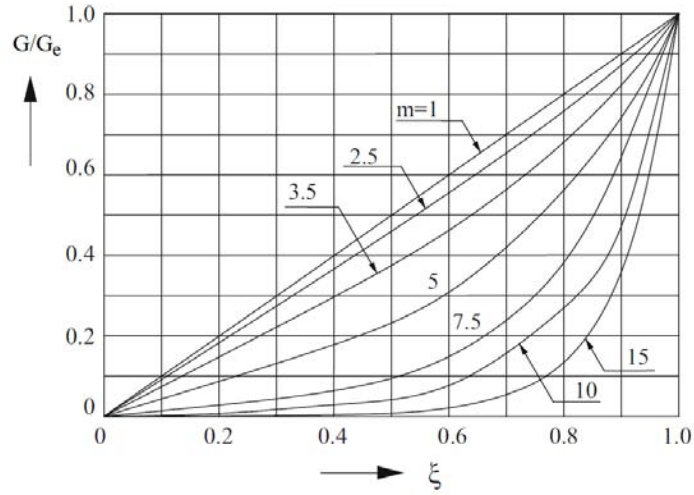


Figure 2.10: Distribution of current density G along the radius, referred to the value G_e at the surface. [3]

if $m \leq 1$,

$$\frac{H}{H_e} \approx 1, \quad \frac{G}{G_e} \approx \xi, \quad \text{and} \quad \frac{w}{w_e} \approx \xi^2;$$

if $m \gg 1$,

$$\begin{cases} \frac{H}{H_e} \approx \frac{G}{G_e} \approx \frac{e^{x/\delta}}{\sqrt{1 - (x/r_e)}}, \\ \frac{w}{w_e} \approx \frac{e^{2x/\delta}}{\sqrt{1 - (x/r_e)}}, \end{cases}$$

having defined the distance from the surface as $x = r_e - r$.

2.2.2 Induced power and equivalent impedance of the system

The imaginary and real part of the outward flux of the complex *Poynting vector*, through the outer surface of the cylinder (having radius r_e and length ℓ), is used as a way to determine the active and reactive power induced in the workpiece. The Poynting vector $\dot{\mathbf{p}}$ is defined as follows:

$$\dot{\mathbf{p}} = \dot{\mathbf{E}} \cdot \dot{\mathbf{H}} \quad (2.20)$$

with: $\dot{\mathbf{H}}$ is the conjugate of complex vector $\dot{\mathbf{H}}$.

Recalling the fact that $\dot{\mathbf{E}}_e$ and $\dot{\mathbf{H}}_e$ are vector perpendicular to each other, the active P_w and reactive Q_w power transmitted to the workpiece are determined as

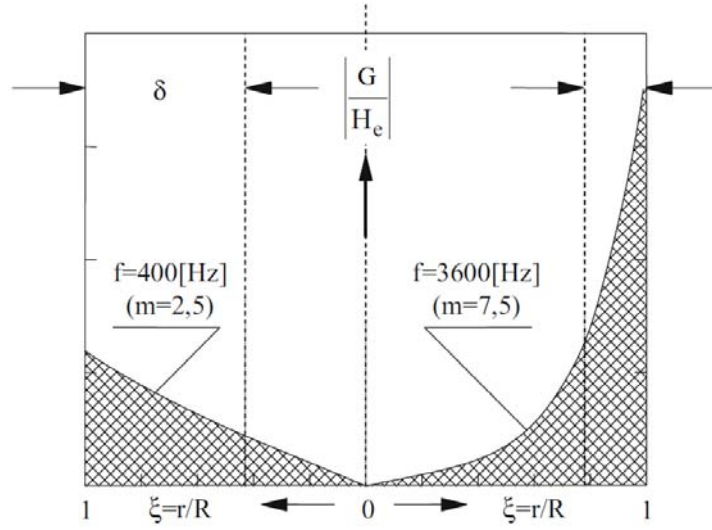


Figure 2.11: Influence of frequency on the induced current density distribution, keeping the value \dot{H}_e constant. [3]

follows:

$$P_w + jQ_w = \int_S \dot{\mathbf{p}} \cdot \mathbf{n} dS = -2\pi r_e \ell \dot{E}_e \dot{H}_e \quad .$$

Substituting the (2.11), evaluated in $\xi = 1$, in the previous expression, it results:

$$\begin{aligned} P_w + jQ_w &= (2\pi r_e \ell) H_e^2 \frac{m}{r_e} \rho (P + jQ) \\ &= (2\pi r_e \ell) H_e^2 \sqrt{2} \frac{\rho}{\delta} (P + jQ), \end{aligned} \quad (2.21)$$

where, in the second expression the relationship between m and δ (i.e. $\delta = \sqrt{2} r_e / m$) has been applied. It follows that, a few important parameters can be extrapolated from the above equations. They are defined as:

$$\begin{aligned} A + jB &= \frac{2}{m} (P + jQ) && \text{with trends shown in Fig. 2.9;} \\ X_{i0} &= \omega N^2 \frac{\mu_0 \pi r_e^2 \alpha^2}{\ell} && \text{reactance of empty coil } (\Omega). \end{aligned}$$

It may result useful to rephrase the Eq (2.21) including these last defined parameters, as follows:

$$\begin{aligned} P_w + jQ_w &= \frac{N^2 I^2}{\ell^2} \sqrt{2} \frac{\rho}{\delta} (P + jQ) (2\pi r_e \ell) \frac{m}{m} \\ &= \frac{X_{i0}}{\alpha^2} \mu (A + jB) I^2 \quad . \end{aligned} \quad (2.22)$$

Induced active and reactive power are key parameters for the specification of an induction heating system, however, the *equivalent impedance of the induction-load system* is of fundamental important for the design of the inductor coil. For its

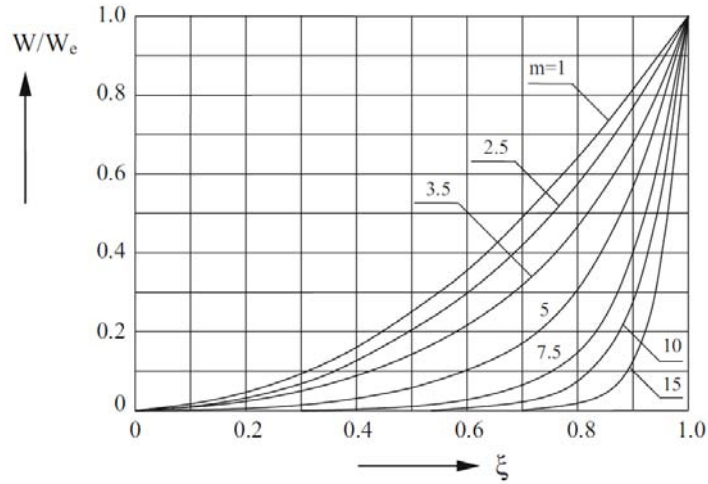


Figure 2.12: Distribution of specific power w along the radius, referred to the value w_e at the surface. [3]

evaluation, a series equivalent circuit is preferred than the parallel one. Neglecting the inductor own resistance, or rather assuming the inductor ideal, the reactive power Q_a in the air gap between cylinder and coil must be taken into account. In this region the magnetic field intensity \dot{H}_e is constant. Therefore, the estimation of the total impedance starts from the evaluation of the magnetic energy density in the air gap:

$$w_m = \frac{1}{2}HB$$

and then integrating in the air gap volume, it results:

$$W_m = w_m \cdot \pi(r_i^2 - r_e^2)\ell = \frac{1}{2}\mu_0 H_e^2 \pi(r_i^2 - r_e^2)\ell \quad . \quad (2.23)$$

The magnetic energy can also be expressed in function of the current as $W_m = \frac{1}{2}L_a I^2$, likewise the reactive power as $Q_a = XI^2$. So that, Q_a can be written, using the Eq. (2.23), as:

$$Q_a = 2\omega W_m = \frac{X_i 0}{\alpha^2}(\alpha^2 - 1)I^2 \quad (2.24)$$

The reactive power is detrimental for almost all the electrical applications as it influences the voltage levels and that's why it's a common practice to minimize it. Focusing on Eq. (2.24), it is notable that the parameter $\alpha = r_e/r_i$ weights on the value of the reactive power. A low value of α permits to minimize the reactive power absorbed by the system, however, its value shouldn't be too small for avoiding excessive thermal radiation from the hot load towards the inductor, reducing its efficiency. The value of α is, in general, between 1,1 and 1,4.

At this point, combining the Eqs. (2.22) and (2.24) *the total active and reactive*

power of the ideal induction-load system results:

$$\dot{S} = P_w + j(Q_w + Q_a) = \frac{X_{i0}}{\alpha^2} \left\{ \mu A + j[\alpha^2 - (1 - \mu B)] \right\} \cdot I^2 \quad . \quad (2.25)$$

Since the total complex power \dot{S} has been already characterized, it remains to define *the equivalent impedance* at the ideal coil clamps, defined as follows:

$$\dot{Z}_{e0} = R'_w + j(X_a + X'_w) = R'_w + j(X_{i0} - \Delta X) \quad . \quad (2.26)$$

The expression of \dot{Z}_{e0} is compound of the following parameters:

$$\begin{aligned} R'_w &= \frac{X_{i0}}{\alpha^2} \mu A = N^2 \rho \frac{2\pi r_e}{\ell \delta} \sqrt{2} P && \text{resistance of the load at the inductor terminals,} \\ X'_w &= \frac{X_{i0}}{\alpha^2} \mu B && \text{reactance of the load at the inductor terminals,} \\ X_a &= X_{i0}(\alpha^2 - 1) && \text{reactance relating to the reactive power } Q_a, \\ \Delta X &= \frac{X_{i0}}{\alpha^2} (1 - \mu B) && \text{variation of inductor reactance from loaded to} \\ &&& \text{unloaded conditions.} \end{aligned}$$

Accordingly, a positive value of ΔX gives rise to an overall reduction of the equivalent impedance. A non-magnetic material, since the value of the parameter B is minor to one with $m > 2$, presents a reduction of the total reactance passing from unloaded to loaded inductor. Conversely, a ferromagnetic material, since $\mu \gg 1$, could present an increase of the total reactance, depending on the value of B (see Fig. 2.9). Since $B = 2mQ$, it depends mainly on the frequency. At low frequencies, the total reactance tends to increase ($\Delta X < 0$). However, for high values of "m" the effect of demagnetization currents is high enough to induce a decrease of the overall reactance ($\Delta X > 0$).

The equivalent impedance of the inductor-load system can also be computed knowing the total flux concatenating the coil. Continuing to adopt the hypothesis of neglecting the own resistance of the inductor, designating with:

$$\begin{aligned} \dot{V}_0 & \text{ voltage at coil terminals (V);} \\ \dot{Z}_{e0} & \text{ equivalent impedance of the system } (\dot{\Omega}); \\ \dot{\Phi} & \text{ total flux concatenated with the coil (Wb);} \\ \dot{\Phi}_w & \text{ total flux concatenated with the load (Wb)} \\ \dot{\Phi}_a & \text{ flux in the air gap between coil and load (Wb),} \end{aligned}$$

it leads to:

$$\dot{Z}_{e0} = \frac{\dot{V}_0}{\dot{I}} = \frac{j\omega N \dot{\Phi}}{\dot{I}} = \frac{j\omega N (\dot{\Phi}_w + \dot{\Phi}_a)}{\dot{I}} \quad . \quad (2.27)$$

The flux related to the load can be computed, recalling Eq. (2.9), from the

following expression:

$$\dot{\Phi}_w = \mu\mu_0 \int_0^{r_e} 2\pi r \dot{H} dr = \frac{2\pi r_e^2 \mu\mu_0 \dot{H}_e}{J_0(\sqrt{-j}m)} \int_0^1 \xi J_0(\sqrt{-j}m) d\xi \quad .$$

Recalling that

$$\int_0^1 \xi J_0(\beta\xi) d\xi = \frac{J_1(\beta)}{\beta},$$

the previous relationship becomes:

$$\begin{aligned} \dot{\Phi}_w &= 2\pi r_e^2 \mu\mu_0 \dot{H}_e \frac{J_1(\sqrt{-j}m)}{\sqrt{-j}m J_0(\sqrt{-j}m)} \\ &= \mu\mu_0 \dot{H}_e \pi \delta^2 m (Q - jP) \end{aligned} \quad (2.28)$$

where P and Q parameters determined by Eq. (2.17).

The flux within the air gap simply is:

$$\dot{\Phi}_a = \mu_0 \dot{H}_e \pi (r_i^2 - r_e^2) = \mu_0 \dot{H}_e \pi r_e^2 (\alpha^2 - 1) \quad . \quad (2.29)$$

Thus, substituting in Eq. (2.27) the relationships (2.28) and (2.29), it obtains once more Eq. (2.26)

$$\dot{Z}_{e0} = \frac{X_{i0}}{\alpha^2} \left\{ \mu A + j[\alpha^2 - (\mu B)] \right\} \quad . \quad (2.30)$$

2.2.3 Heating of hollow workpieces

General solution Let's examine a cylindrical induction-load system of infinite axial length, as in the previous sections. However, in this paragraph a hollow workpiece, hereafter named also *tube*, is taken into account. The exciting magnetic field presents different intensities at the external and internal surfaces, respectively \dot{H}_e and \dot{H}_i (see Fig. 2.13).

The evaluation of the electromagnetic magnitudes is developed as done in the case of a solid load. Adding the following parameters at those already defined

r, r_i, r_e current, internal and external radii of the tube (m),
 $s = r_e - r_i$ tube thickness (m)

hence: $m_r = \frac{\sqrt{2}r}{\delta}$; $m_i = \frac{\sqrt{2}r_i}{\delta}$; $m_e = \frac{\sqrt{2}r_e}{\delta}$; $\Delta m = \frac{\sqrt{2}s}{\delta}$.

By that, it's possible to rewrite the Eqs. (2.7) and (2.8) respectively as follow:

$$\begin{aligned} \frac{d^2 \dot{H}}{dr^2} + \frac{1}{r} \frac{d\dot{H}}{dr} - j \frac{\omega\mu\mu_0}{\rho} \dot{H} &= 0 \\ \dot{H} &= \dot{C}_1 J_0(\sqrt{-j}m_r) + \dot{C}_2 Y_0(\sqrt{-j}m_r) \quad . \end{aligned}$$

Introducing the boundary conditions of the magnetic field on the last expression,

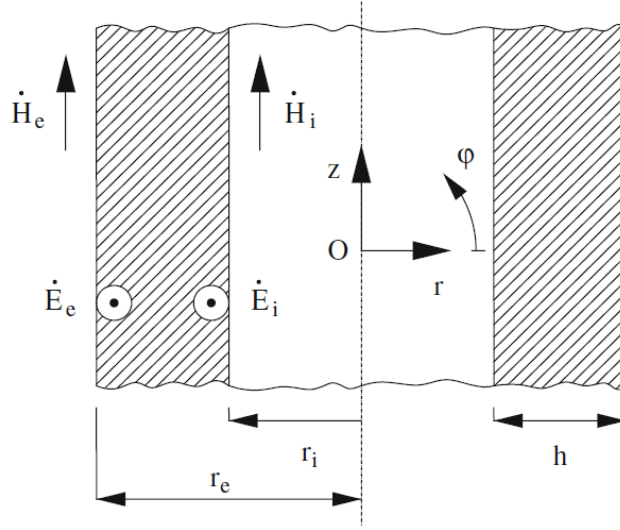


Figure 2.13: Hollow cylinder load placed in axial magnetic field [4].

it results:

$$\begin{cases} \dot{H}_e = \dot{C}_1 J_0(\sqrt{-j}m_e) + \dot{C}_2 Y_0(\sqrt{-j}m_e) \\ \dot{H}_i = \dot{C}_1 J_0(\sqrt{-j}m_i) + \dot{C}_2 Y_0(\sqrt{-j}m_i) \end{cases} \quad (2.31)$$

and³

$$C_1 = \frac{\begin{vmatrix} \dot{H}_e & Y_0(\sqrt{-j}m_e) \\ \dot{H}_i & Y_0(\sqrt{-j}m_i) \end{vmatrix}}{F_{00}(m_i, m_e)} = \frac{\dot{H}_e Y_0(\sqrt{-j}m_i) - \dot{H}_i Y_0(\sqrt{-j}m_e)}{F_{00}(m_i, m_e)}$$

$$C_2 = \frac{\begin{vmatrix} J_0(\sqrt{-j}m_e) & \dot{H}_e \\ J_0(\sqrt{-j}m_i) & \dot{H}_i \end{vmatrix}}{F_{00}(m_i, m_e)} = \frac{\dot{H}_e J_0(\sqrt{-j}m_i) - \dot{H}_i J_0(\sqrt{-j}m_e)}{F_{00}(m_i, m_e)}$$

where F_{00} is defined as

$$F_{00}(m_i, m_e) = \begin{vmatrix} J_0(\sqrt{-j}m_e) & Y_0(\sqrt{-j}m_e) \\ J_0(\sqrt{-j}m_i) & Y_0(\sqrt{-j}m_i) \end{vmatrix} \quad (2.32)$$

$$= J_0(\sqrt{-j}m_e)Y_0(\sqrt{-j}m_i) - Y_0(\sqrt{-j}m_e)J_0(\sqrt{-j}m_i) \quad (2.33)$$

³Using the Cramer's algorithm used for solving linear equation systems having exactly one solution.

Substituting \dot{C}_1 and \dot{C}_2 in the Eq. (2.8) rewritten above, we finally get:

$$\dot{H} = \dot{H}_e \frac{F_{00}(m_i, m_r)}{F_{00}(m_i, m_e)} - \dot{H}_i \frac{F_{00}(m_e, m_r)}{F_{00}(m_i, m_e)} \quad (2.34)$$

In line with Eq. (2.11) and computing the derivate of Eq. (2.34), the electric field intensity is:

$$\dot{E} = -\rho \frac{d\dot{H}}{dr} = \sqrt{-2j} \frac{\rho}{\delta} \left[\dot{H}_e \frac{F_{01}(m_i, m_r)}{F_{00}(m_i, m_e)} - \dot{H}_i \frac{F_{01}(m_e, m_r)}{F_{00}(m_i, m_e)} \right] \quad (2.35)$$

with:

$$F_{01}(x, y) = J_1(\sqrt{-j}y)Y_0(\sqrt{-j}x) - Y_1(\sqrt{-j}y)J_0(\sqrt{-j}x) \quad (2.36)$$

Tubes heated with external inductors This case differs from the general one by the absence of an internal exciting magnetic field. This case, which is the closest to the real system examined in this study, is characterized by an inductor surrounding a tube. The magnetic field intensity \dot{H}_e on the outer layer of the load is generated by the coil, whereas the internal magnetic field \dot{H}_i is unknown and supposed constant. For determining the value of the magnetic field inside the cavity of the tube, the *e.m.f* induced in an ideal conductor, placed at the radius $r = r_i$, must be equal to the derivate of the concatenated flux.

We obtain

$$\oint \dot{E} d\ell = 2\pi r_i \dot{E}_i = -j\omega \dot{\Phi}_i = -j\omega \mu_0 \dot{H}_i \pi r_i^2$$

or better, using Eq. (2.34):

$$\dot{E}_i = -j \frac{\omega \mu_0 r_i}{2} \dot{H}_i = \sqrt{-2j} \frac{\rho}{\delta} \left[\dot{H}_e \frac{F_{01}(m_i, m_i)}{F_{00}(m_i, m_e)} - \dot{H}_i \frac{F_{01}(m_e, m_r)}{F_{00}(m_i, m_e)} \right] \quad (2.37)$$

Taking into consideration that is:

$$F_{01}(m_i, m_i) = F_{01}(x, x) = \frac{2}{\sqrt{-j}\pi x},$$

and elaborating the previous expression, we obtain the ratio between the magnetic field intensity on the surface over the one on the cavity surface:

$$\frac{\dot{H}_e}{\dot{H}_i} = -j \frac{\pi m_i^2}{2\mu} [F_{00}(m_i, m_e) + F_{01}(m_e, m_i)]$$

By mean of Eqs. (2.34) and (2.35) one can evaluate the relative distribution along the thickness of tube wall of the magnetic field strength and the current density $\dot{G} = \dot{E}/\rho$. In Fig. 2.14 are shown a few qualitative distribution curves. The below

diagram emphasizes that at relative low frequency (f_1), the magnetic field intensity H remains steady within the thickness of the tube while G varies linearly. By contrast, at high frequency (f_4) the trends can be approximated with exponentials.

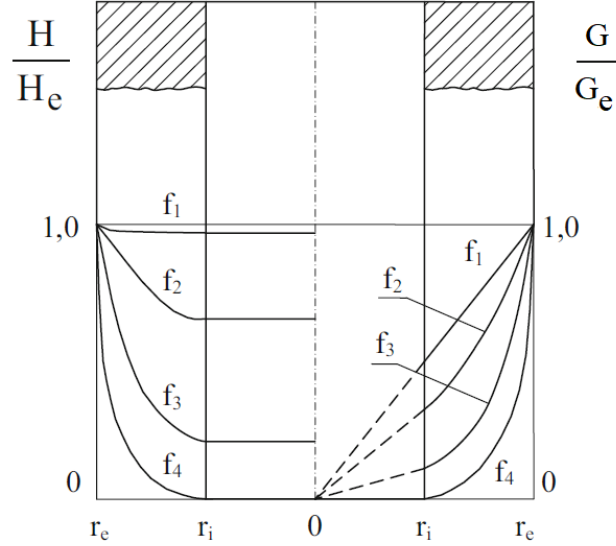


Figure 2.14: Magnetic field intensity and current density relative distributions in tubes heated with external coils [4].

Computing the flux of the Poynting vector through the external surface of the hollow load, as already done in Sect. 2.2.2 for a massif one, the active and reactive power can be expressed as follows:

$$P_w + jQ_w = -\dot{E}_e \dot{H}_e 2\pi r_e \ell = H_e^2 \frac{\rho}{\delta} \sqrt{2} (P_{te} + jQ_{te}) 2\pi r_e \ell \quad (2.38)$$

being:

$$P_{te} + jQ_{te} = -\sqrt{-j} \left[\frac{F_{01}(m_i, m_e)}{F_{00}(m_i, m_e)} - \frac{\dot{H}_i}{\dot{H}_e} \frac{F_{01}(m_e, m_e)}{F_{00}(m_i, m_e)} \right] \quad (2.39)$$

coefficients of active and reactive power in tubes heated with an external inductor. The values of P_{te} and Q_{te} are illustrated by the curves of Fig. 2.15 for non-magnetic material ($\mu = 1$) as a function of m_e and $\Delta m = \sqrt{2}/\delta$.

They underline that:

- the active power increase almost linearly till a maximum, for low values of Δm because of the insignificant influence of induced currents;
- as Δm tends to 1, the demagnetization effect of the induced currents overcomes and P_{te} drops after the maximum;
- likewise in a solid cylinder, the power coefficients tend to the value $1/\sqrt{2}$

for high values of Δm and the induced currents within the wall becomes exponential.

In the case of a ferromagnetic hollow workpiece, when the penetration depth is comparable with the thickness of the load wall, only numerical methods are available [4]. The variations of resistivity and magnetic permeability during heating can affect results considerably. A series of numerical simulations denote that the increase of H_e permits to obtain more uniform distributions of current and power density in the wall thickness [4]. This effect is attestable to the fact that, increasing H_e , the relative magnetic permeability μ_r falls off and so the penetration depth δ_e increase. By contrast, setting higher frequency, the penetration depth δ_e lessens causing more irregular distributions of current and power density in the tube wall.

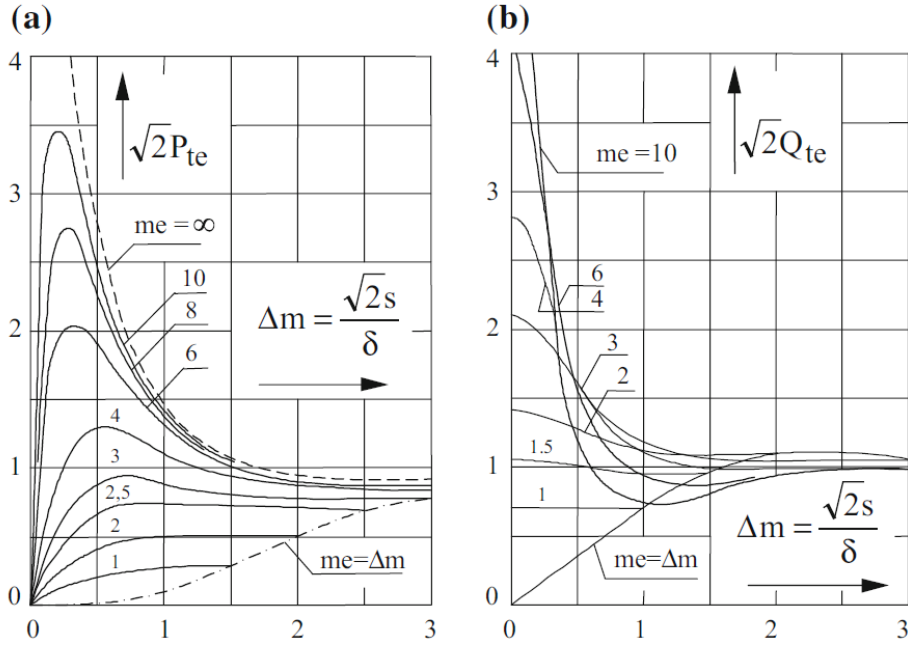


Figure 2.15: Coefficient of active power (a) and reactive power (b) power in tubes heated with external inductors ($m_e = \sqrt{2}r_e/\delta$) [3].

2.3 Electrical parameters

2.3.1 Resistance and reactance of inductor

For the evaluation of its own resistance and internal reactance, the coil can be approximate as a hollow cylinder, assumed as a portion of an infinitely long configuration. In addition, it is subdivided in N adjacent turns of rectangular cross section, as shown in Fig. 2.16b. This configuration differs from the one analysed in

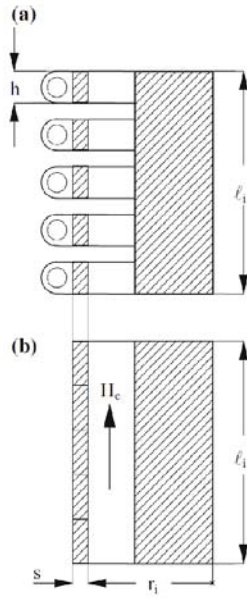


Figure 2.16: Schematization of the inductor coil for calculation of its own resistance R_i and internal reactance X_{ii} [3].

the previous paragraph by the internal position of the exciting magnetic field and by the absence of the one at the external surface ($H_e = 0$). With reference to these new conditions, Eqs. (2.34) and (2.35) can be readapted as follow:

$$\begin{cases} \frac{\dot{H}}{\dot{H}_i} = \frac{F_{00}(m_r, m_e)}{F_{00}(m_i, m_e)} \\ \frac{\dot{E}}{\dot{H}_i} = -\sqrt{-2j} \frac{\rho}{\delta} \frac{F_{01}(m_e, m_r)}{F_{00}(m_i, m_e)}, \end{cases} \quad (2.40)$$

bearing in mind that the functions $F_{00}(x, y)$ and $F_{01}(x, y)$ are still defined by Eqs. (2.33), (2.36) and $F_{00}(x, y) = -F_{00}(y, x)$. Accordingly, the active and reactive power can be calculated, as already done before, by the evaluation of the flux of the Poynting vector flowing outwards through the surface of the cylinder of radius r_i . The complex power in a section of the cylinder is so determined as

$$P_w + jQ_w = \dot{E}_i \dot{H}_i 2\pi r_i l = H_i^2 \frac{\rho}{\delta} \sqrt{2} (P_{ti} + jQ_{ti}) 2\pi r_i l \quad (2.41)$$

with:

$$P_{ti} + jQ_{ti} = -\sqrt{-j} \left[\frac{F_{01}(m_i, m_e)}{F_{00}(m_i, m_e)} \right]$$

The values of power coefficients are given by the diagrams of Fig. 2.17, for different values of m_i . The previous relationships and the below diagram can be used for the evaluation of the electrical parameters of induction coil.

Therefore, new denominations for the parameters have been adopted in order to

avoid misunderstandings

$$\begin{aligned}
\dot{H}_e &= \frac{NI}{\ell_i} && \text{intensity of magnetic field applied (A/m)} \\
s &&& \text{radial thickness of the conductor composing the coil (m)} \\
r_i &&& \text{internal radius of inductor (m) being } r_e = r_i + s \\
\rho_i &&& \text{resistivity of the coil material } (\Omega \text{ m}) \\
\delta_i &= \sqrt{\frac{2\rho_i}{\omega\mu_0}} && \text{coil's penetration (m) depth}
\end{aligned}$$

$$m_r = \frac{\sqrt{2}r}{\delta_i} \quad m_i = \frac{\sqrt{2}r_i}{\delta_i} \quad m_e = \frac{\sqrt{2}r_e}{\delta_i} \quad \Delta m = m_e - m_i$$

In specific, the active and reactive power P_i and Q_i generated in the inductor volume, can be written as:

$$P_i + jQ_i = H_e^2 \frac{\rho_i}{\delta_i} (A_i + jB_i) 2\pi r_i \ell \quad . \quad (2.42)$$

By mean of the latter expression and recalling that a series equivalent circuit has been adopted, the own resistance R_i and the internal reactance X_{ii} of the inductor can be evaluated as:

$$\begin{cases}
R_i = \frac{P_i}{I^2} = N^2 \rho_i \frac{2\pi r_i}{\ell_i \delta_i} A_i k_i = X_{i0} \frac{\delta_i}{r_i} A_i k_i \\
X_{ii} = \frac{Q_i}{I^2} = N^2 \rho_i \frac{2\pi r_i}{\ell_i \delta_i} B_i = X_{i0} \frac{\delta_i}{r_i} B_i
\end{cases} \quad (2.43)$$

with k_i coefficient, greater than one, that takes into account the real distribution of the coil turns which have an axial separation from each other. It is equal to $k_i = 4\ell_i/N \cdot \pi d$ for conductors of circular cross-section and $k_i = \ell_i/N \cdot h$ for rectangular cross-section ones. The resistance is proportional of k_i wherefore higher is the value of k_i the more conductive material is used to build the inductor up and so, bigger is the resistance.

From the curves of Fig. 2.17, it's possible to point out that:

- considering all the other conditions equal, the losses in the inductor reach a minimum for $\frac{s}{\delta_i} = \frac{\pi}{2} \approx 1.57$ and then tend to a constant value, slightly above the least value, for increasing Δm .
- in order to keep the losses as low as possible, the thickness s should be selected to ensure that $s/\delta_i \geq 1.57$ in relation to the frequency. In addition to that, the value of k_i should be close to unit.

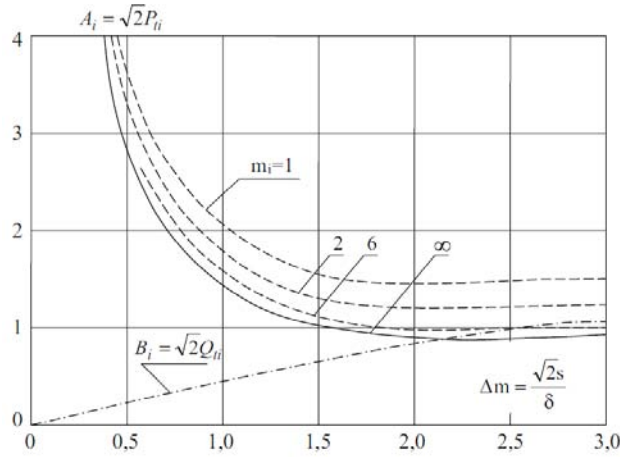


Figure 2.17: Active and reactive power coefficients in tubes with internal exciting magnetic field [3]

2.3.2 Electrical efficiency

The electrical efficiency of a system is generally defined as the ratio between the useful power output and the total electrical power absorbed. In the case of an induction heating system the electrical efficiency η_e can be calculated dividing the power transformed into heat within the workpiece and the total active power absorbed by the inductor. With reference to the previous notation, it is:

$$\eta_e = \frac{R'_w I^2}{(R'_w + R_i) I^2} = \frac{R'_w}{R'_w + R_i} = \frac{1}{1 + \frac{R_i}{R'_w}} \quad (2.44)$$

$$= \frac{1}{1 + \frac{r_i \ell \delta A_i k_i}{r_e \ell_i \delta_i \sqrt{2P}}} = \frac{1}{1 + \alpha \frac{\ell}{\ell_i} \sqrt{\frac{\rho_i}{\rho \mu} \frac{A_i k_i}{\sqrt{2P}}}} \quad (2.45)$$

where the expression of R'_w and R_i , given by Eqs. (2.26) and (2.43), have been introduced.

The latest expression highlighted the dependence of the electrical efficiency on the next parameters:

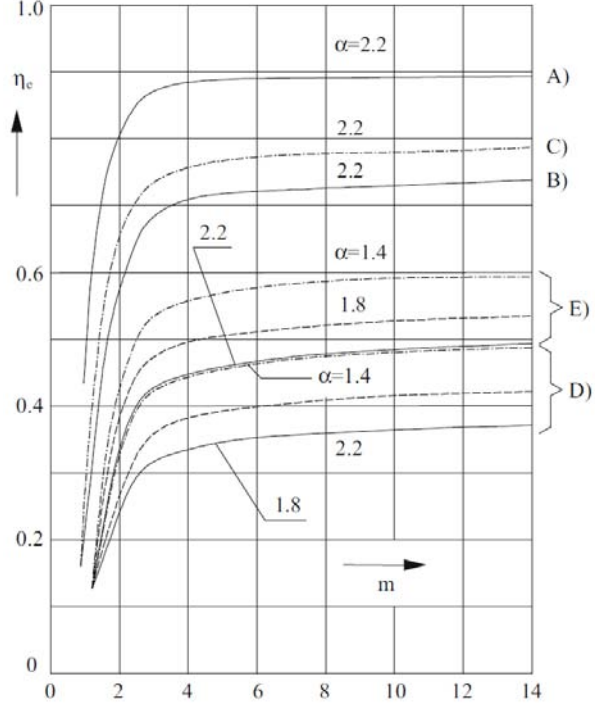
- the ratio between the internal diameter of the inductor and the diameter of the workpiece, named coupling ratio $\alpha = r_e/r_i$ as well as the ratio between their axial length ℓ/ℓ_i ;
- the material resistivity of the inductor ρ_i ;
- the permeability μ and resistivity ρ of the load material;
- the characteristic parameters of the inductor coil $A_i k_i$
- the P coefficient which depends on the ratio $m = \sqrt{2}/\delta$.

Optimizing the inductor design, or rather adopting high value of m ($A_i \approx 1$,

$P \approx 1/\sqrt{2}$), $\ell_i = \ell$ and $k_i \approx 1$, the maximum electrical efficiency achievable is defined by:

$$\eta_{e\max} = \frac{1}{1 + \alpha \sqrt{\frac{\rho_i}{\rho\mu}}} \quad (2.46)$$

Figure 2.18: Electrical efficiency of the inductor-load system as a function of m . **A** steel heated from 0 to 800 °C; **B** steel from 800 to 1200 °C; **C** steel from 0 to 1200 °C; **D** aluminium heated from 0 to 500 °C and copper to 800 °C; **E** brass from 0 to 800 °C [3]



A first analysis of the curves in Fig. 2.18 reveals that for $m > 2.5$ the electrical efficiency is almost independent on the frequency, whereas for smaller m it sinks to very low values. That's why, in practical applications, m should never be lower than 2.5. Besides this, the electrical efficiency depends strongly on α , decreasing significantly with the increase of it, specially when heating non-magnetic materials or magnetic materials over Curie point. Accordingly, workpieces with very different diameters should be heated with tailor-designed inductors. Furthermore, it can be pointed out that electrical efficiency reaches interesting values with carbon steels or materials with high resistivity.

2.3.3 Power and Quality factor

The power factor, or $\cos \varphi$, is defined as the ratio between the active power transferred to the load and the apparent power absorbed by the inductor-load system. The $\cos \varphi$ express the power utilization efficiency and it can be determined, neglecting X_{ii} , and using the Eqs. (2.26) and (2.43) and the expression of η_e , as

follows:

$$\cos \varphi = \frac{R_i + R'_w}{\sqrt{(R_i + R'_w)^2 + (X_{i0} - \Delta X)^2}} \quad (2.47)$$

$$= \frac{1}{\sqrt{1 + \left[\frac{\alpha^2 - (1 - \mu B)}{\mu A} \eta_e \right]^2}} \quad (2.48)$$

The *Merit* or *Quality Factor* is whereas defined as the ratio between reactive and active power at the inductor terminals. It can be evaluated with the following:

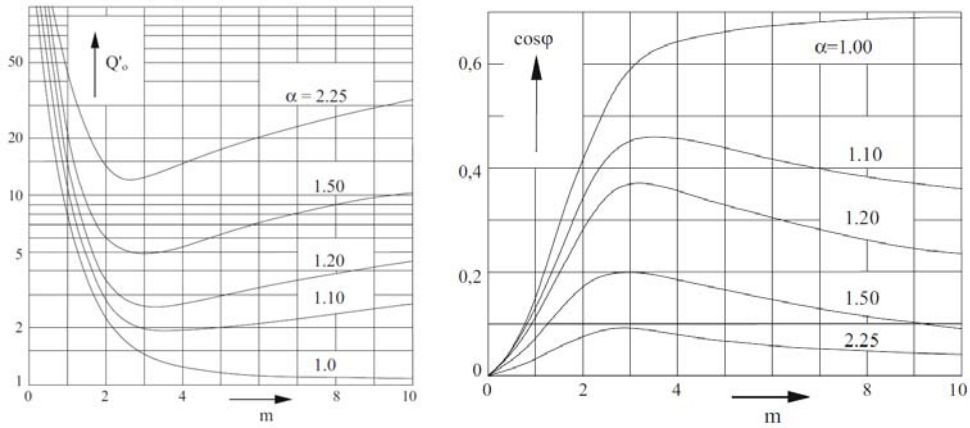
$$Q_0 = \frac{X_{i0} - \Delta X}{R_i + R'_w} = \frac{X_{i0} - X_{i0} \frac{(1 - \mu B)}{\alpha^2}}{R'_w} \eta_e \quad (2.49)$$

$$= \frac{\alpha^2 - (1 - \mu B)}{\mu A} \eta_e = Q'_0 \eta_e \quad (2.50)$$

where Q'_0 is the quality factor related to an ideal inductor system.

Consequently, the power factor can be written as a function of the ideal quality factor, resulting

$$\cos \varphi = \frac{1}{\sqrt{1 + (Q'_0 \eta_e)^2}} \quad .$$



(a) Ideal quality factor Q'_0 for non-magnetic materials (b) Power factor for non-magnetic material and ideal inductor-load system

Figure 2.19: Quality and Power factors as a function of m

From Fig. 2.19b we can notice that the inductor-load system is characterized by low values of $\cos \varphi$, even for different values of α . It can be, therefore, pointed out that it's necessary to compensate for the prevalent reactive power by connecting an array of capacitors in parallel to the inductor. This power factor correction leads to an improvement of the operating condition of the converter, which can be affected by

strong variations of impedance of the inductor-load system during heating [3].

2.3.4 Thermal transient analysis

Since the power distributions previously examined tend always to produce uneven heating in the workpiece cross-section, the interest in the behaviour of thermal transient becomes crucial. The main industrial applications of induction heating systems can be sorted in relation to the temperature distribution within the load at the end of heating. The main categories are [3]:

- *localized heating*, characterized by elevate temperature differentials among different points of the cross-section and required, for instance, in hardening;
- *uniform heating*, conversely characterized by a temperature distribution as uniform as possible and required for through heating processes prior hot working.

The process analysed in this work is part of those applications that aim to obtain an uniform heating. However, for a complete understanding of the subject, a general thermal transient analysis is carried out.

Recalling the already used assumptions of a cylindrical load having a length much greater than its diameter, the heat transmission occurs only in the radial direction. In addition, all the thermal parameters defining the cylindrical load are assumed constant. The thermal diffusion is ruled by the *Fourier equation* which is expressed, for cylindrical coordinates and for the hypothesis done, as follows:

$$\frac{\partial \theta}{\partial t} = k \left(\frac{\partial^2 \theta}{\partial r^2} + \frac{1}{r} \frac{\partial \theta}{\partial r} \right) + \frac{w(r)}{c\gamma} \quad (2.51)$$

where

θ	temperature in °C, at a radius r at time t
$k = \lambda/c\gamma$	diffusivity of the load material in m^2/s ;
λ	thermal conductivity of the load material in $W/m^\circ C$;
c	specific heat of the load material in $J/kg^\circ C$;
γ	specific weight of the load material in kg/m^3 ;
$w(r)$	specific power induced within the load in W/m^3 .

For the solution of Fourier equation,⁴ the below simplifying hypotheses of null initial load temperature and adiabatic heating (i.e no thermal losses) are adopted:

⁴In order to obtain the final differential equation(2.51) the laplacian operator in cylindrical coordinates has been recalled. It is $\nabla^2 \theta = \frac{1}{r} \frac{\partial}{\partial r} \left(r \frac{\partial \theta}{\partial r} \right) + \frac{1}{r^2} \frac{\partial^2 \theta}{\partial \varphi^2} + \frac{\partial^2 \theta}{\partial z^2}$.

- $\theta(r) = 0$, for $t = 0$ (initial condition);
- $\frac{\partial \theta}{\partial r} = 0$, for $t > 0$ and $r = r_e$ (boundary condition).

In order to obtain a general solution, a few dimensionless parameters have been introduced, with the following denotation:

- $\xi = \frac{r}{r_e}$ dimensionless radius;
- $\tau = \frac{kt}{r_e^2}$ dimensionless time;
- $\Theta = \frac{2\pi\lambda}{P_u}\theta$.

P_u is the power induced, per unit of axial length, in the load (W/m), defined as:

$$P_u = \int_0^{r_e} 2\pi r w(r) dr = 2\pi \int_0^1 \xi w(\xi) d\xi \quad .$$

Now, Fourier equation and its initial and boundary conditions can be written as a function of this new parameters as:

$$\frac{\partial \Theta}{\partial \tau} = \frac{\partial^2 \Theta}{\partial \xi^2} + \frac{1}{\xi} \frac{\partial \Theta}{\partial \xi} + \Psi(\xi) \text{ for } 0 \leq \xi \leq 1 \quad (2.52)$$

$$\begin{cases} \Theta(\xi) = 0, \text{ for } \tau = 0 \\ \frac{\partial \Theta}{\partial \xi} = 0, \text{ for } \tau > 0 \text{ and } \xi = 1. \end{cases} \quad (2.53)$$

In the latter equation, the term related to the specific power has been rewritten as $\Psi(\xi)$ which can be defined as: \int_{min}^{max}

$$\Psi(\xi) = \frac{2\pi r_e^2}{P_u} w(r) = \frac{w(\xi)}{\int_0^1 \xi w(\xi) d\xi},$$

therefore, recalling Eq.(2.18), it results

$$\Psi(\xi) = m \frac{ber'^2(m\xi) + bei'^2(m\xi)}{ber m ber' m + bei m bei' m} \quad . \quad (2.54)$$

In the literature, a solution of Eq.(2.52), referred to the aforementioned conditions, is presented as an infinite series of terms calculated thanks to the Laplace transformation. Taking into account complexity of the solution and variations of the material load parameters during heating, assuming $\Psi(\xi)$ constant is a rough approximation. For this reason, it results convenient to refer to easier solutions. By simplifying the expression of w/w_e is possible to obtain a qualitative trend of thermal transient

within the load cross-section.

Because of the much more interest in it, only the thermal transient for *quasi uniform heating* will be discussed.

Focus on through-heating The only way to achieve a fairly uniform distribution of temperature in the load cross-section is represented by a process in which the heating transient ceases in the zone of *linear temperature increase*, after an initial exponential rise. In order to obtain such linear transient in every point of the load cross-section with the same rate, the following condition has to be satisfied:

$$\pi r^2 c \gamma \frac{\partial \theta}{\partial t} = 2\pi r \lambda \frac{\partial \theta}{\partial r} + \int_0^r w \pi r w(r) dr \quad .$$

This expression can be explain as follows: a linear growth of temperature in every point of the cylinder cross-section occurs when the power required to rise the temperature of a cylinder, with radius r and unitary length, at constant rate $(\partial \theta / \partial t)$ results equal to the sum of the power conduced through its lateral surface plus the power induced in the cylindrical load.

Introducing the dimensionless parameters ξ, Θ, τ in the previous relationship, it results:

$$\frac{\partial \Theta}{\partial \tau} = \frac{4\pi r_e^2}{P_u \xi^2} \int_0^\xi \xi w(\xi) s \xi + \frac{2}{\xi} \frac{\partial \Theta}{\partial \xi} \quad . \quad (2.55)$$

The constant rate of growth of the temperature can be evaluated considering a cylinder of unitary axial length, radius r_e and the total power P_u converted into heat in it. By that, the relation is:

$$P_u = \pi r_e^2 c \gamma \frac{\partial \theta}{\partial t}$$

that, replacing the dimensionless parameters, gives:

$$\frac{\partial \Theta}{\partial \tau} = 2. \quad (2.56)$$

Now, from the equality of Eqs. (2.54) and (2.56) it's possible to write the following expression, independent on τ :

$$\frac{\partial \Theta}{\partial \xi} = \xi - \frac{1}{\xi} \frac{\int_0^\xi \xi w(\xi) d\xi}{\int_0^1 \xi w(\xi) d\xi}, \quad (2.57)$$

which permits to know the distribution of Θ as a function of ξ in the zone of temperature linear growth.

At this point, by substituting in Eq. (2.57) the (2.18) and computing the integrals,

one yields:

$$\frac{\partial \Theta}{\partial \xi} = \xi - \frac{\text{ber } m\xi \text{ber}' m\xi + \text{bei } m\xi \text{bei}' m\xi}{\text{ber } m \text{ber}' m + \text{bei } m \text{bei}' m}$$

and with a new integration one obtains:

$$\Theta = \frac{1}{2}\xi^2 - \frac{\text{ber}^2 m\xi + \text{bei}^2 m\xi}{2m(\text{ber } m \text{ber}' m + \text{bei } m \text{bei}' m)} + C.$$

In order to evaluate the integration constant C , one can denote with $\Theta_a = \Theta(\xi = 0)$ or rather the value on the axis, and obtains:

$$\Theta = \Theta_a + \frac{1}{2}\left[\xi^2 - \frac{\text{ber}^2 m\xi + \text{bei}^2 m\xi - 1}{m(\text{ber } m \text{ber}' m + \text{bei } m \text{bei}' m)}\right] \quad (2.58)$$

The temperature values obtained with Eq. (2.58) yield to the curves of Fig. 2.20 given for different values of m .

Specifically, for $m \rightarrow \infty$ the trend is parabolic:

$$\Theta - \Theta_a = \frac{1}{2}\xi^2,$$

and the differential between load surface ($\Theta = \Theta_s$ for $\xi = 1$) and axis temperature results:

$$\Theta_s - \Theta_a = \frac{1}{2}.$$

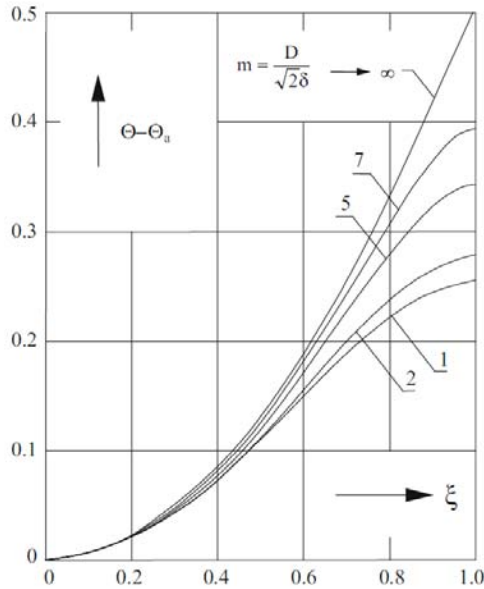


Figure 2.20: Radial temperature distribution during the linear temperature increase [3]

For finite values of m the differential temperature is lower, considering the same

power converted into heat within the load, once again computing that distribution with $\xi = 1$. So that, it yields to:

$$\Theta_s - \Theta_a = \frac{1}{2}F(m) \quad (2.59)$$

having defined $F(m)$ as follows:

$$F(m) = 1 - \frac{ber^2 m + bei^2 m - 1}{m(ber m ber' m + bei m bei' m)}. \quad (2.60)$$

The term $F(m)$ is a correction factor to the case of local surface heating, which take into account that the heat is generated inside the load. Its values are given by Fig. 2.21a, as a function of m .

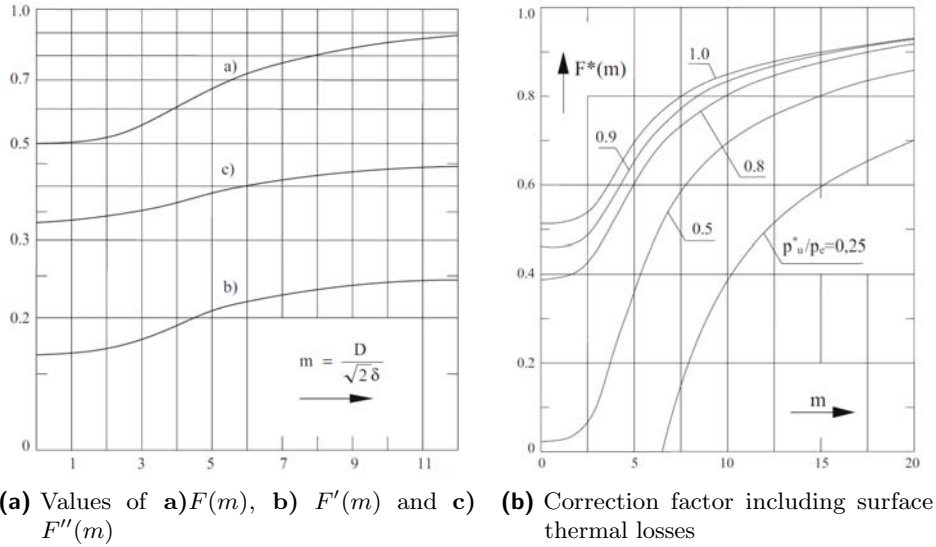


Figure 2.21: Correction factor without and with surface thermal losses

For the evaluation of the heating time is preferable to refer to an average temperature rather than the surface one. Its dimensionless value can be calculated with the following:

$$\Theta_m = \frac{2\pi\lambda}{P_u}\theta_m = 2 \int_0^1 \Theta\xi d\xi,$$

that brings to

$$\Theta_m = \Theta_a + F'(m) \quad (2.61)$$

The parameter $F'(m)$ is defined as

$$F'(m) = \frac{1}{4} - \frac{ber m bei' m - bei m ber' m - m/2}{m^2(ber m bei' m + bei m ber' m)}. \quad (2.62)$$

Under the assumption of no thermal losses and from Eq. (2.56), the average temperature can also be written as:

$$\Theta_m = 2\tau, \quad (2.63)$$

so Eq. (2.58) becomes:

$$\Theta = 2\tau - F'(m) + \frac{1}{2} \left(\xi^2 - \frac{ber^2 m \xi + bei^2 m \xi - 1}{m(ber m ber' m + bei m bei' m)} \right). \quad (2.64)$$

From the latter, it results easy to evaluate the surface value, being $\xi = 1$, as:

$$\Theta_s = 2\tau - F'(m) + \frac{1}{2} F(m). \quad (2.65)$$

The so-called *through heating* processes are characterized by a specific on final surface temperature θ_s with a set temperature difference between surface and axis ($\theta_s - \theta_a$). Using Eqs. (2.59) and (2.65) it's possible to calculate the heating time t and the power P_u required for satisfying the requirements of a uniform heating process. Introducing the relative temperature differential $\varepsilon = \frac{\theta_s - \theta_a}{\theta_s}$, one can reformulate the dimensionless time as:

$$\tau = \frac{F(m)}{4\varepsilon} [1 - \varepsilon F''(m)] \quad \left(\text{with } F''(m) = 1 - 2 \frac{F'(m)}{F(m)} \right), \quad (2.66)$$

which finally brings to the following expression of t and P_u :

$$\begin{cases} t = r_e^2 \frac{F(m)}{4k\varepsilon} [1 - \varepsilon F''(m)] = r_e^2 \frac{\pi c \gamma}{P_u} \theta_s [1 - \varepsilon F''(m)] \\ P_u = \frac{4\pi\lambda}{F(m)} (\theta_s - \theta_a) = 4\pi\lambda \frac{\varepsilon}{F(m)} \theta_s \end{cases} \quad (2.67)$$

These last equations underline that for small values of ε (in the range of 0.05 – 0.10) the term $\varepsilon F''(m)$ is insignificant compared to unit. Actually, it only considers that the evaluation of the heating time is done referring to the external surface rather than to an average value, like shown in Fig. 2.22. The relationship for the heating time emphasize the influence on it of the value of ε and the m , then frequency.

Further deduction can be carried out from Eqs.(2.67):

- the increasing the frequency brings to an increase of $F(m)$ and, as a result, lessens the power P_u and enlarges the heating time t , keeping constant all other conditions;
- adopting a constant value of frequency, a set final average temperature with a smaller ε can be achieved reducing P_u and longer the heating time;

- the only parameter on which is possible to act in order to adjust ε , is the frequency, then m and $F(m)$, since the final temperature θ_s and heating time are assigned and permit to define of the power P_u ;
- vice versa, for given values of θ_s and ε , based on process requirements, it's feasible to enlarge P_u and reduce the heating time only by lessening the value of $F(m)$, adopting a suitable frequency.

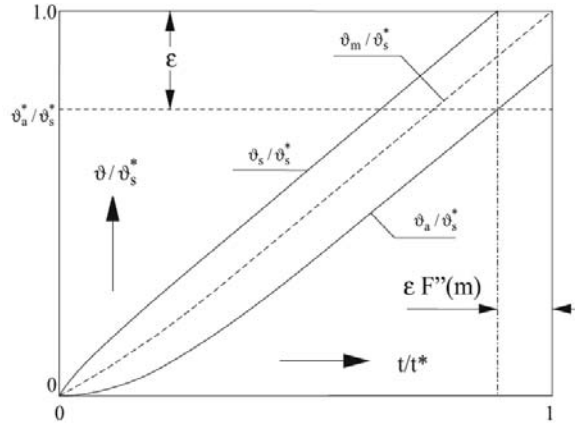


Figure 2.22: Thermal transient in uniform heating of non-magnetic workpieces, neglecting surface losses (* – final temperatures)[3]

In the foregoing analysis, the surface losses have been neglected. However, on the one hand, they limit the useful power and so enlarge the heating time; on the other hand, they give rise to a smaller temperature differential in the cross-section.

Under these circumstances, a second evaluation of the heating time can be done, referring to the useful power P_u^* through the following expressions:

$$\begin{cases} t = r_e^2 \frac{\pi c \gamma}{P_u^*} \theta_s [\varepsilon F''(m)] \\ (\theta_s - \theta_a) = \frac{P_u^*}{4\pi \lambda} F''(m), \end{cases} \quad (2.68)$$

where:

- $P_u^* = P_u - 2\pi r_e p_i$ useful power (W/m)
- p_i surface losses (W/m²)
- $F''(m)$ correction term as a function of P_u^*/P_u (see Fig. 2.21b)

2.4 Variations of material features

In all the previous paragraphs, the analysis has been carried out under the assumption that physical characteristics of the load (i.e electrical resistivity ρ , specific

heat c and thermal conductivity λ) and thermal exchange conditions did not change during the heating process. However, it's well known that the heating process is directly influence by the variations of these features with temperature. Furthermore, in magnetic steels the variation of magnetic permeability with temperature and field intensity contribute significantly to affect the process.

The foregoing assumption is therefore acceptable only within a limited range of temperature, in which appropriate weighted values can be accepted. Since the importance of considering such variations, in the following, the consequences will be examined qualitatively. A heating transitory characterized by a temperature increase from θ_1 to θ_2 will be taken as a reference, with the simplifying hypothesis of neglecting the uneven temperature distribution in the load cross-section. The parameters related to initial θ_1 and final θ_2 temperature will be hereafter denoted with the subscript 1 and 2 .

In connection with these last considerations and on the base of the previous expressions, the following can be drawn:

- the penetration depth δ is modified in the ratio:

$$\frac{\delta_2}{\delta_1} = \sqrt{\frac{\rho_2 \mu_1}{\rho_1 \mu_2}};$$

- m changes according to:

$$\frac{m_2}{m_1} = \frac{\delta_1}{\delta_2} = \sqrt{\frac{\rho_1 \mu_2}{\rho_2 \mu_1}};$$

- the eddy currents distribution varies as a function of m , as shown in Fig. 2.10;
- the surface induced current density G_e , with constant exciting magnetic field, varies during heating in the ratio:

$$\frac{G_{2e}}{G_{1e}} = \frac{m_2}{m_1} \sqrt{\frac{(P^2 + Q^2)_2}{(P^2 + Q^2)_1}};$$

- the specific power changes in the ratio:

$$\frac{w_{2e}}{w_{1e}} = \frac{\rho_2}{\rho_1} \left(\frac{G_{2e}}{G_{1e}} \right)^2 = \frac{\rho_2}{\rho_1} \left(\frac{m_2}{m_1} \right)^2 \frac{(P^2 + Q^2)_2}{(P^2 + Q^2)_1};$$

- with constant inductor current (i.e constant field intensity), the transferred active power varies in the ratio:

$$\frac{P_{2w}}{P_{1w}} = \frac{A(m_2)}{A(m_1)} = \frac{\rho_2 m_1 P(m_2)}{\rho_1 m_2 P(m_1)};$$

- the electrical efficiency as well as the power factor is affected by the variation of m as already analysed in 2.3.2.

Ferromagnetic materials In addition to the variation of resistivity with temperature $\rho(\theta) = \rho_0(1 + \alpha_0 \theta)$, (see Fig. 2.23), these materials exhibit a strong dependence of magnetic permeability on field intensity and temperature, as shown in Fig. 2.24.

$$\mu = \mu(H, \theta),$$

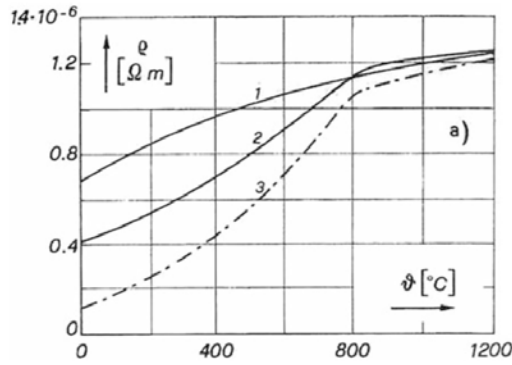


Figure 2.23: Resistivity variation of different steels (1 Inox 18CrNi8; 2 Rapid steel; Carbon steel 0.06 %) [3]

Electrical resistivity varies in a non-linear way with temperature for magnetic material. In fact, curves 2 and 3 show that resistivity increase rapidly in the range of temperature between 0 to 800 °C whereas, at higher temperature, the rate of growth decrease.

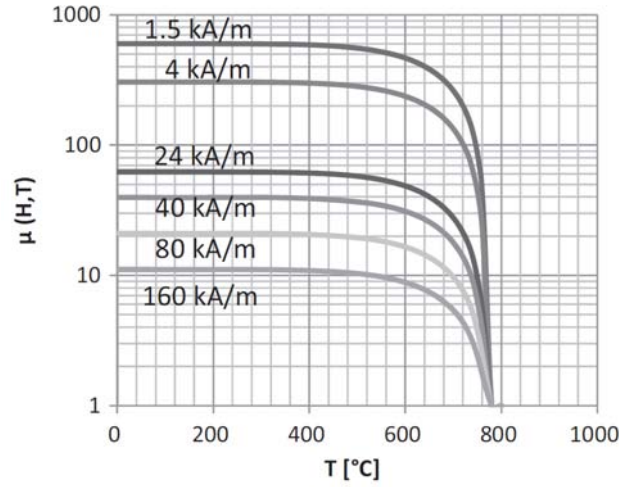
The value of permeability is always referred to value at room temperature $\mu_{20^\circ\text{C}}$. It undergoes variations which depend not only on the field intensity but also on the material carbon content. Since, in induction applications the field intensity is usually elevate, the value of $\mu_{20^\circ\text{C}}$ can be estimated by mean of:

$$\mu_{20^\circ\text{C}} = 1 + \frac{B_s}{H} \approx 1 + \frac{14000 \div 16000}{H}$$

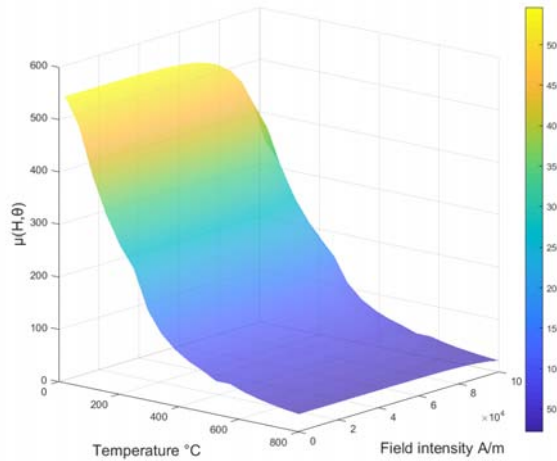
with H is in A/cm and B_s , the magnetic saturation induction, in Gauss. This is just one of the several formulae proposed by different authors.

The magnetic permeability is fairly constant for temperature in the range from 20 °C to 500 ÷ 600 °C, whereas it goes down to the values 1 in the proximity of the Curie Point. As a result, it's possible to approximate a heating process with a final temperature beyond the Curie Point, at which correspond a temperature of $\approx 750 \div 800^\circ\text{C}$, with two distinct processes with constant parameters. The first one, below 750 °C, is characterized by average resistivity $\rho_A \approx 50 \div 60 \cdot 10^{-8} \Omega\text{m}$ and μ_A

whereas the second, related to heating period above Curie Point, has permeability $\mu_B = 1$ and resistivity $\rho_B \approx 100 \div 120 \cdot 10^{-8} \Omega\text{m}$.



(a) Values for *steel C45* [5]



(b) Surface plot showing values for *steel C45*, evaluated by a model presented in [5]

Figure 2.24: Relative magnetic permeability depending on temperature and magnetic field intensity

Considering a common value of exciting field H_e for these applications and using the latter parameters values, one earns:

$$\frac{\delta_A}{\delta_B} = \frac{m_B}{m_A} = \sqrt{\frac{f_B}{f_A}} \approx \frac{1}{20} \div \frac{1}{10}; \quad (2.69)$$

and recalling that, it should be $m \geq 2.5$ for guarantee a high electrical efficiency,

one obtains:

$$\begin{cases} m_A \geq (10 \div 20) \cdot 2.5; \\ \frac{P_{uB}}{P_{uA}} \approx \left(\frac{H_{eB}}{H_{eA}}\right)^2 \sqrt{\frac{f_B}{f_A}} \sqrt{\frac{\rho_A}{\rho_B \mu_A}} \left(\frac{P_B}{P_A}\right) \frac{1}{1.37} \end{cases} \quad (2.70)$$

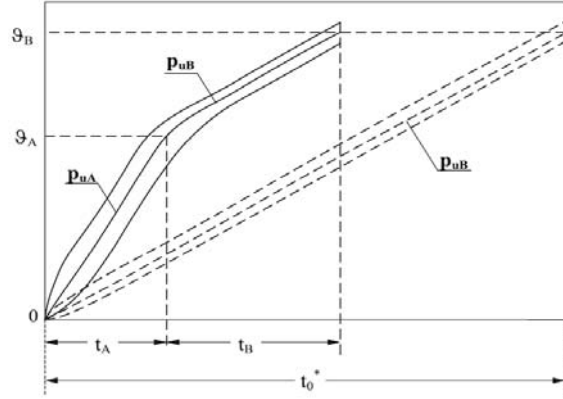
From the diagram of Fig. 2.25, one can write:

$$t_0 = t_A + t_B \approx \pi r_e^2 \left[\frac{c_A \theta_A}{P_{uA}} + \frac{c_B (\theta_B - \theta_A)}{P_{uB}} \right]. \quad (2.71)$$

However, the calculation of t_0 could be done considering that the integrated average values of c_A and c_B are roughly the same and physical characteristics are equal to the ones of a load heated with constant power P_{uB} , above the Curie temperature. Denoting with t_0^* the duration of the equivalent transient, it results:

$$\begin{cases} \frac{t_0}{t_0^*} = \frac{t_A + t_B}{t_0^*} \approx \frac{\frac{c_A \theta_A}{P_{uA}} + \frac{c_B (\theta_B - \theta_A)}{P_{uB}}}{\frac{c_B \theta_B}{P_{uB}}} \approx \frac{\theta_A \frac{P_{uB}}{P_{uA}} + (\theta_B - \theta_A)}{\theta_B} \\ \frac{t_A}{t_B} \approx \frac{\theta_A}{\theta_B - \theta_A} \frac{P_{uB}}{P_{uA}} \end{cases} \quad (2.72)$$

Figure 2.25: Schematization of the heating transient of a magnetic billet, for the evaluation of heating time [3]



Assuming that at the end of heating transient m_B has to be not lower than 2.2 for not compromise the electrical efficiency and introducing the integrated average values of ρ_A and ρ_B , we get:

$$\frac{P_{uB}}{P_{uA}} \approx 0.15 \div 0.20; \quad \frac{t_A}{t_B} \approx 0.20 \div 0.36; \quad \frac{t_0}{t_0^*} \approx 0.47 \div 0.53.$$

Thus, for an inductor with uniform ampere-turns, the following consideration can be drawn:

- usually, the value of m has to be set elevated (≥ 25) under the Curie point;
- the power induced under the Curie point is much bigger than the one above it;

- the heating time can be roughly evaluated by taking half of the time of an ideal heating with constant P_{uB} .

Actually the value of m varies during the heating time. It decreases gradually from a high initial value (with power and current distributed in a thin external layer) to smaller and smaller values. As a result, the induced current, and so the power density distribution pierces gradually into the workpiece.

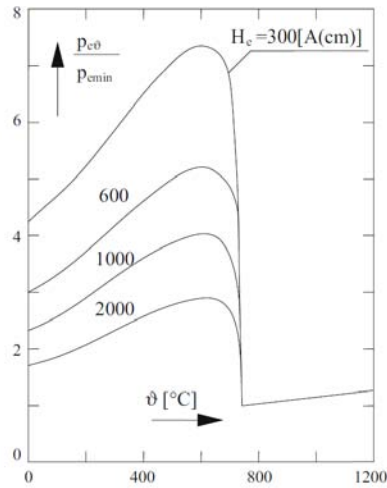


Figure 2.26: Relative variation of specific power with temperature in the case of heating a magnetic steel [3]

In Figure 2.26 is illustrated how the power induced in the workpiece changes with the temperature, for different values of H_e . The first part of curves is characterized by a nearly linear increase because of the trend of resistivity, which grows within that temperature range, whereas permeability stays nearly constant. After reaching the maximum, the power suddenly falls down since the decrease of permeability value is prevalent with respect to the increase of resistivity.

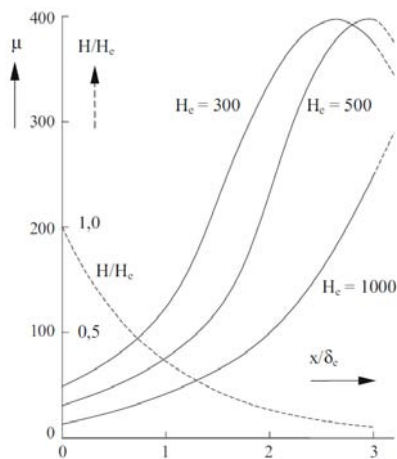


Figure 2.27: Distribution of μ within a magnetic load due to local field intensity ($\rho = \text{const}$; $x = \text{distance from the surface}$; H_e in A/cm [3])

Accordingly to these last considerations, also μ is uniform along the radius of the load, and its distribution is illustrated in Fig.2.27. Different authors developed

non-linear analytical theories, considering such permeability distribution, stating that the induced power, with μ variable as function of the magnetic field intensity, is about 1.37 times bigger than the value computed with a constant value referred to the surface field intensity, whereas the reactive power don't undergo significant variation [3, 4]. The distribution of power and current density changes too. In fact, the increase of permeability in comparison with surface value permits to the electromagnetic wave to penetrate deeper into the load. In addition to that, a second phenomenon contributes to modify their theoretical distribution. During heating, at the transition that occurs at the Curie point, the hotter layers turn into non-magnetic whereas the underlying ones are still magnetic. Thus, the induced current distribution as a double exponential trend, as shown in Fig. 2.28, related to the different values of δ in the non-magnetic and magnetic regions.

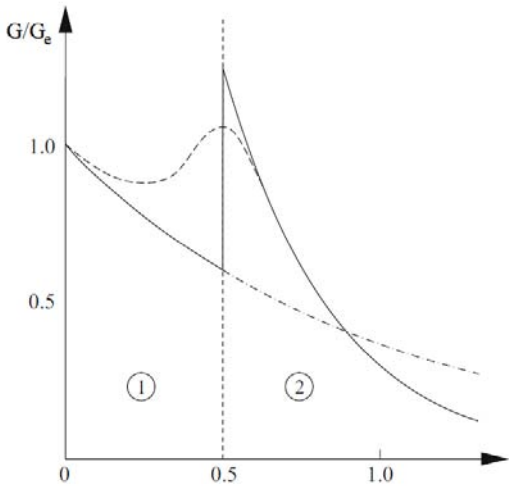


Figure 2.28: Qualitative current density distribution at Curie transition with reference to the surface value (1 non-magnetic; 2 magnetic) [3]

Chapter 3

Numerical approach

3.1 *FEA*: Finite Element Analysis

The increasing complexity of engineering problems, ranging from structural to electromagnetic analyses, gave rise to the need to implement and develop new computational methodologies substituting the conventional analytical methods. Nowadays, the most widely used one is the *Finite Element Method*, hereafter FEM. As suggested by the name, this method employs piecewise approximation in which the continuum domain of interest is parted into multiple sub regions called finite elements. The *discretization* of the domain enables to solve each single element independently and later, obtain the overall solution for the continuum domain merging these finite elements outcomes [6]. At the end of the process, if the obtained results are not satisfying, the analysis can be repeated with different parameters. The finite element method is the most flexible one to solve partial differential equations (*PDEs*) problems, for instance electromagnetic and thermal analysis.

3.1.1 Electromagnetic and thermal physics characterization

This section aims to present how electromagnetic and thermal problems can be characterized, focusing on the PDEs which have to be solved. Starting by the electromagnetic analysis is well known that fields can be subdivided into two main classes: time independent (static) and time varying.

Quasi stationary fields – Low frequency

Slow varying and period fields having a frequency up to 10 kHz are considered to be part of the quasi-stationary category. Most of the physical problems in energy engineering can be described by quasi-static phenomena [7]. The crucial consideration to do to categorize a problem in this class deal with the displacement

current. The discriminant is the wavelength λ of the system considered in the frequency domain. If it is large compared to the physical dimension of the system, neglecting the displacement current is reasonable and the field can be considered as quasi-static.

Recalling the Maxwell equations and the constitutional relations is possible to obtain a partial differentiate equation, function of the magnetic vector potential \mathbf{A} , called *A-formulation*.

$$\nabla \cdot \mathbf{D} = \rho_c \quad (3.1a)$$

$$\nabla \cdot \mathbf{B} = 0 \quad (3.1b)$$

$$\nabla \times \mathbf{E} = -\frac{\partial \mathbf{B}}{\partial t} \quad (3.1c)$$

$$\nabla \times \mathbf{H} = -\frac{\partial \mathbf{D}}{\partial t} + \mathbf{G} \quad (3.1d)$$

$$\mathbf{D} = \varepsilon \varepsilon_0 \mathbf{E} \quad (3.1e)$$

$$\mathbf{B} = \mu \mu_0 \mathbf{H} \quad (3.1f)$$

$$\mathbf{G} = \sigma \mathbf{E} \quad (3.1g)$$

Magneto static fields are well described by Ampere's law, neglecting the displacement term $\frac{\partial \mathbf{D}}{\partial t}$, and the magnetic flux conservation law. Thus, using the definition of the magnetic vector potential $\mathbf{B} = \nabla \times \mathbf{A}$, the Faraday's law (3.1c) can be written as follow:

$$\nabla \times \mathbf{E} = -\frac{\partial}{\partial t}(\nabla \times \mathbf{A}). \quad (3.2)$$

Additionally, employing the Ohm's law referred to eddy currents G_e evaluation, it yields to:

$$\mathbf{G}_e = \sigma \mathbf{E} = -\sigma \frac{\partial \mathbf{A}}{\partial t}.$$

Then, combining the last two relationships, the Ampere's law can be reformulate for the quasi stationary magnetic field in time domain, obtaining the following A-formulation:

$$\nabla \times \left(\frac{1}{\mu \mu_0} \nabla \times \mathbf{A} \right) + \sigma \frac{\partial \mathbf{A}}{\partial t} = \mathbf{G}$$

and applying the vector identity $\nabla \times \nabla \times \mathbf{A} = \nabla(\nabla \cdot \mathbf{A}) - \nabla^2 \mathbf{A}$ it becomes,

$$\frac{1}{\mu \mu_0} \left(-\nabla^2 \mathbf{A} + \nabla(\nabla \cdot \mathbf{A}) \right) + \sigma \frac{\partial \mathbf{A}}{\partial t} = \mathbf{G}.$$

Finally, assuming the Coulomb gauge condition ($\nabla \cdot \mathbf{A} = 0$) we obtain the desired equation, a function of the magnetic vector potential:

$$\nabla^2 \mathbf{A} - \mu \mu_0 \sigma \frac{\partial \mathbf{A}}{\partial t} = -\mu \mu_0 \mathbf{G}. \quad (3.3)$$

Now, presuming a sinusoidal excitation current, characterized by an angular frequency ω , the A-formulation is defined in the frequency domain instead of time-domain and allows to solve eddy currents problems:

$$\nabla^2 \mathbf{A} - j\omega\mu\mu_0\sigma\mathbf{A} = -\mu\mu_0\mathbf{G}, \quad (3.4)$$

being $\frac{\partial \mathbf{A}}{\partial t} = j\omega\mathbf{A}$.

Magnetodynamic fields (*waves*) – High frequency

In general, when the displacement current has to be taken into account, the Ampere's law is in the form of Eq. (3.1d). It follows that, by substituting the aforementioned definition of the magnetic vector potential and recalling the Gauss's law (3.1a), we obtain:

$$\nabla \times \nabla \times \mathbf{A} = \mu\mu_0\mathbf{G} + \mu\mu_0 \frac{\partial \mathbf{D}}{\partial t}$$

then, using the relation (3.1e) and the vector identity it results

$$\nabla(\nabla \cdot \mathbf{A}) - \nabla^2 \mathbf{A} = \mu\mu_0\mathbf{G} + \mu\mu_0\varepsilon\varepsilon_0 \frac{\partial \mathbf{E}}{\partial t}. \quad (3.5)$$

Now, recalling the Faraday-Lenz's law as written in Eq. (3.2) we can write the following relationship:

$$\nabla \times \left(\mathbf{E} + \frac{\partial \mathbf{A}}{\partial t} \right) = 0.$$

Seeing that the term between brackets is *irrotational*, it results to be equal to the gradient of a scalar function; the scalar potential V

$$\mathbf{E} + \frac{\partial \mathbf{A}}{\partial t} = -\nabla V. \quad (3.6)$$

Substituting the Eq. (3.6) into Eq. (3.5) we obtain:

$$\nabla(\nabla \cdot \mathbf{A}) - \nabla^2 \mathbf{A} = \mu\mu_0\mathbf{G} - \mu\mu_0\varepsilon\varepsilon_0 \nabla \frac{\partial V}{\partial t} - \mu\mu_0\varepsilon\varepsilon_0 \frac{\partial^2 \mathbf{A}}{\partial t^2}$$

and assuming the Lorentz condition

$$\nabla \cdot \mathbf{A} = -\mu\mu_0\varepsilon\varepsilon_0 \frac{\partial V}{\partial t}$$

leads to the first wave equation

$$\nabla^2 \mathbf{A} - \mu\mu_0\varepsilon\varepsilon_0 \frac{\partial^2 \mathbf{A}}{\partial t^2} = -\mu\mu_0\mathbf{G}. \quad (3.7)$$

In addition, substituting into Eq. (3.1a) Eqs. (3.6) and (3.1e) we obtain the second wave equation as follows:

$$\nabla^2 V - \mu\mu_0\varepsilon\varepsilon_0 \frac{\partial^2 V}{\partial t^2} = \frac{\rho}{\varepsilon\varepsilon_0} \quad (3.8)$$

with ρ volumetric charge density, as in the Gauss' law.

Equations (3.7) and (3.8) are known as *non-homogeneous wave equations*. Together with the Lorentz conditions, these two equations are analogous to Maxwell's quartet and valid anywhere. On the left side of them, it figures the unknown function whereas on the right side it's present the well determined source term.

Thermal problems

Heating is a very frequent phenomenon on most of the electromagnetic devices and, in many situations, the temperature evaluation is necessary. It is indispensable to avoid undesirable overheating on structures. However, in particular applications such as electro-heating systems, the thermal analysis permits to improve the design of the device. Heat transfer principles and equations are briefly presented in the following.

First, *conduction* is a thermal process in which the heat is transmitted within the body or between bodies having physical contact. The equation describing this thermal phenomenon is

$$c \frac{\partial T}{\partial t} + \nabla(-\lambda \nabla T) = Q \quad (3.9)$$

known as Fourier's equation where Q is the *thermal source volumetric density* (i.e Joule effect source $Q = G^2/\sigma$) expressed in W/m^3 . Because λ is supposed constant, Eq. (3.9) can be rewritten as follow:

$$\nabla^2 T - \frac{c}{\lambda} \frac{\partial T}{\partial t} = -\frac{Q}{\lambda}.$$

This formulation of the Fourier's equation results very similar to Eq. (3.7) and therefore it can be solved similarly.

Then, *convection* takes place when a fluid contacts a heated solid body. In the natural convection phenomenon, heat exchange occurs due to fluid particles movements adjacent to the hot surface. These particles flows are triggered by the density gradient that arises at the contact zone. Conversely, in the forced convection, the heat exchange is induced by using a fan or a pump. However, for both the convection phenomena, the heat exchange is well described by the following equation:

$$\lambda \frac{\partial T}{\partial t} \cdot \vec{n} = -h(T - T_a) \quad (3.10)$$

called Newton's equation where h is the convection heat transfer coefficient in $\text{W}/\text{m}^2\text{C}$. It depends on fluid properties, velocity and geometry of the hot body.

Finally, every body at a higher temperature than 0 kelvin emits electromagnetic waves, therefore, they contribute at the *radiation* heat exchange phenomenon. The transfer of heat between two different bodies, one at temperature T and a second at T_a is described by the following equation:

$$\lambda \frac{\partial T}{\partial t} \cdot \vec{n} = -\varepsilon\gamma, (T^4 - T_a^4),$$

where ε is the emissivity of the emitting body and γ the Stephan Boltzmann constant in $\text{W}/\text{m}^2\text{K}^4$.

Commonly, all these three phenomena occur simultaneously making the heat exchange a complex phenomenon to analyse without using a computational approach.

3.1.2 Solving PDEs

Regularly, only for simple cases or under restrictive hypothesis is possible to obtain a direct analytic PDE's solution. For the solutions of precise and realistic models, numerical methods are frequently the only feasible option. The employment of such models aims to solve a PDE on a discrete set of points of the solution domain; an operation called discretization. In order to do so, the solution domain is parted into subregions, subdomain, having the discretization point as vertices. The mesh size of such process is defined as the distance between two adjacent vertices [7]. In addition, the time is also divided into discrete intervals. By that, a *time step* is defined as the time that elapses between two different times at which the solution is evaluated. A system of algebraic equations is then obtained by an approximation, discretization, of the PDE, where the unknowns are the solution values at the discretization points. This system of algebraic equations is therefore solved using direct or iterative techniques on a computer. Since we introduce a discretization error, it is important to comprehend that the discretized step replaces the original equation with a new one and, because of it, even that exact solution of the approximated problem will yield a rough solution of the starting PDE. The numerical scheme has to be stable, convergent and consistent to obtain an acceptable solution. It results stable if the solution remains bounded during the solving procedure; convergent if the numerical solution tends to the real one whilst, the mesh size and the time step tend to zero. Moreover, the scheme is consistent if the *truncation error*¹ tends to zero as well.

¹the truncation error is a quantity measuring the extent to which the true solution satisfies the discrete equation [8]

Calling Φ the unknown function contained in the PDE is important to understand that Φ must satisfy not only the solution in the calculation domain Ω , but also on its surrounded boundary Σ . The choice of the boundary conditions has, therefore, an influence on the final solution. The boundary conditions can be sorted in three main typology:

- 1) *Dirichlet condition*: it consists on fixing an established value of the potential on a specified boundary curve. By mean of that, this chosen curve is characterised by a constant value of the potential hence the equipotential curves are tangent to this benchmark boundary.

The Dirichlet condition can be expressed as:

$$\Phi(r) = f(r) \quad r \text{ on } \Sigma. \quad [7]$$

- 2) *Neumann condition*: this condition consists on setting the normal derivative on a given boundary curve. By imposing this condition, therefore, the equipotential lines cross the boundary in a known way.

The Neumann condition is well described as follows:

$$\frac{\partial \Phi(r)}{\partial n} = g(r) \quad r \text{ on } \Sigma. \quad [7]$$

- 3) *Mixed boundary condition*: this condition is the composition of Dirichlet and Neumann conditions. It is well described as follows:

$$\frac{\partial \Phi(r)}{\partial n} + h(r) \cdot \Phi(r) = w(r) \quad r \text{ on } \Sigma. \quad [7]$$

where $h(r)$ and $w(r)$ are explicit known functions on Σ .

The finite element method offers two different approaches to solve PDE denoted as *variational* approach and *weighted residual* approach. Although by applying them to solve a PDE system, lead to the same set of equations, in the variational one, a function to be minimized is necessary, typically the energy of the system. By contrast, the weighted approach takes into account at first the differential equation of the system, usually in the following form:

$$L(\Phi) - f = 0.$$

Referring to the wave equations (3.7) and (3.8) in the above equation L is a linear operator (for instance ∇^2), f is the known function (for example the source term) and Φ is the unknown function. Furthermore, the precise solution of the system can be expressed by approximate it with a combination of a set of known functions,

weighted by unknown coefficients, following:

$$\Phi_n = \varphi_0 + \sum_{i=1}^n a_i \varphi_i. \quad (3.11)$$

The function φ_0 is generally determined to satisfy Dirichlet boundary condition. Then, introducing the residual R_n is possible to reformulate the weighted approach as follows:

$$L(\Phi_n) - f = R_n, \quad (3.12)$$

where the residual function R varies in the domain Ω . The coefficients a_i are estimate the orthogonalisation of residual R_n on a certain group of n weighing functions w_j . It can be evaluated, for instance, by zeroing the inner product

$$\langle R_n, w_j \rangle = \int_{\Omega} R_n w_j d\Omega = 0 \quad j=1,2,\dots,n. \quad (3.13)$$

One possible solution is imposing $w_j = \varphi_i$ or rather, equating the weighing function and the approximation function. This choice is named *Galerkin method*. Finally, a set of n coinciding linear algebraic equations is obtained and thus can be solved considering proper boundary conditions.

3.2 Ansys Parametric Design Language (APDL)

In this study, the FEA is carried out using the multi-physics simulator software ANSYS®. Especially, a tool of this widely developed software, named APDL (acronym of ANSYS Parametric Design Language), has been chosen to investigate the electro-thermal problem. It enables to perform structural analysis or resolve mechanical problems, however, it permits to solve thermo-structural and electro-thermal tasks.

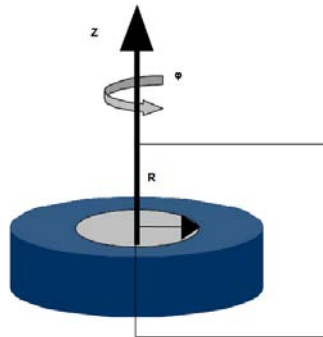


Figure 3.1: Axisymmetric body example [7]

In figure 3.2, the main steps of the script, built on ANSYS © for the pre-processing stage, are highlighted.

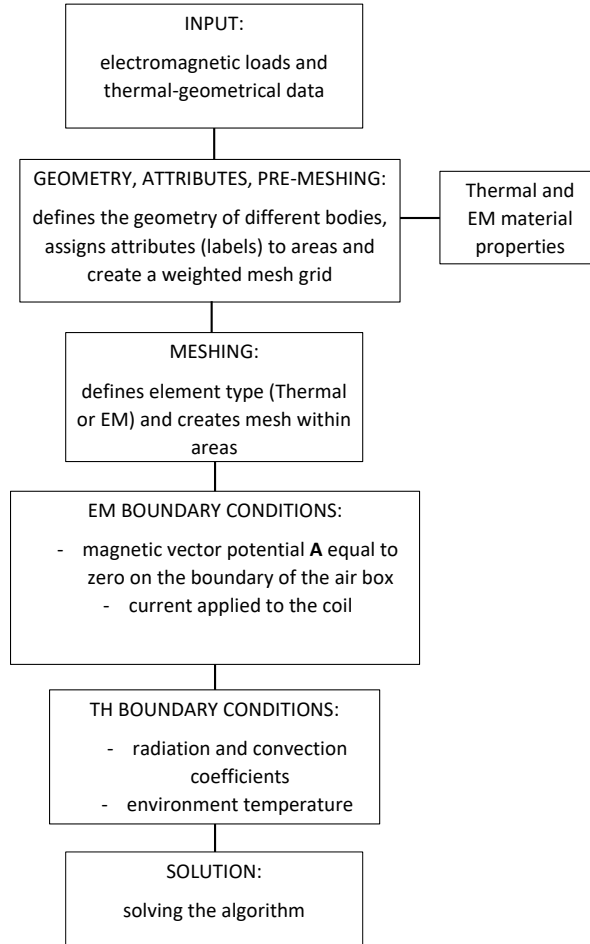


Figure 3.2: Flux diagram of the developed script – pre-processing

Thanks to the geometrical features of the analysed workpiece, the considered model in the investigation is axisymmetric. It means that every phenomenon are supposed as identical on each semi-plane. Thus, the 3D model can be gained by rotation of one semi-plane through a symmetry axis z , as shown in Fig. 3.1. Moreover, this reduction of a 3D problem to a 2D one brings not only geometrical advantages but also it leads to a consistent computational time-saving. Thus, adopting a cylindrical coordinate system (r, φ, z) for a magnetostatic problem leads to rely to

the following conditions:

- the current density has only the azimuthal component G_φ . The associated vector is so $\mathbf{G} = (0, G_\varphi, 0)$ where the only not null component is function of r and z coordinates;
- the magnetic vector potential \mathbf{A} is parallel to vector \mathbf{G} having only the azimuthal component too: $\mathbf{A} = (0, A_\varphi, 0)$;
- the flux density vector \mathbf{B} , being $\mathbf{B} = \nabla \times \mathbf{A}$ has the only component lying on the (r, z) plane. It's expressed as

$$\mathbf{B} = \left(\frac{\partial A_\varphi}{\partial z}, 0, \frac{1}{r} \frac{\partial}{\partial r} (r A_\varphi) \right).$$

To calculate the effects of an alternating current (AC) or voltage excitation in electromagnetic devices and moving conductors the *2D harmonic analysis* has been adopted. The effects involve [9]:

- eddy currents;
- skin effect;
- power loss due to eddy currents;
- forces and torque
- impedance and inductance;
- two contacting bodies with dissimilar mesh.

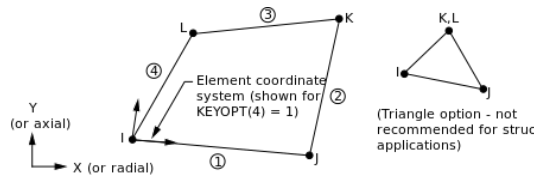
A time-harmonic analysis can be run, for low saturation cases, with assumed constant permeability properties. In moderate to high saturation conditions, it's more interesting obtaining the global electromagnetic force, torque and power losses in a magnetic device under sinusoidal steady-state excitation. On the contrary, the analyst is often less concerned with the actual flux density waveform [9]. Subsequently, an approximate *nonlinear time-harmonic analysis procedure* can be prosecuted. Adopting this analysis procedure a good accuracy prediction of time averaged torque and power loss is obtained and yet at much reduced computational cost compared to the transient time-stepping procedure [9].

The essential principle of the nonlinear time-harmonic analysis consists in replacing the DC (Direct Current) B-H curve with a fictive of effective B-H curve based on an energy equivalent method. Employing this effective B-H curve, the nonlinear transient problem can be validly reduced to a nonlinear time-harmonic one. It follows that, in this nonlinear analysis, all field quantities are sinusoidal at an imposed frequency, and results similar to linear harmonic analysis. However, a nonlinear solution is computed. It should be accentuated that, given a sinusoidal power source, in a nonlinear transient case the magnetic flux density \mathbf{B} has a non-sinusoidal waveform, whereas, in the nonlinear harmonic analysis, \mathbf{B} is assumed

sinusoidal. Moreover, it's not the actual waveform but rather, an approximation to the fundamental time-harmonic of the real B waveform. Hence, the time-averaged outcomes of the analysis, evaluated by the approximated fundamental harmonic of field, are consequent approximations of true values.

The harmonic model uses only A-formulation for eddy-currents regions. Therefore, the choice of element types to use is obliged. In this study, the following type of element has been used for carrying out the 2D harmonic analysis.

PLANE 13: bidimensional element, quadrilateral (4 nodes) or triangular (3 nodes) shaped.



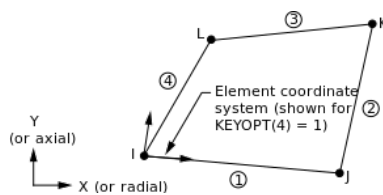
It's defined by up to four *DOF (Degree Of Freedom)* per node: magnetic vector potential (AZ), displacements, temperature or time integrated electric potential [9].

In electrothermal problems, the electromagnetic analysis is strictly coupled with the thermal one. Thus, a *thermal analysis* evaluates not only temperatures but also other time-varying thermal quantities. One possible approach to define time-dependent loads consists of discretizing the load versus time curve into load steps. These method permits to treat each step as a steady-state regime problem. By mean of the steady-state thermal analysis, in each step, temperatures, thermal gradients heat flow rates and heat fluxes, can be evaluated. These thermal quantities are caused by loads that do not vary over time. Such loads include [10]:

- convections;
- radiation;
- heat flow rates;
- heat fluxes (heat flow per unit area);
- heat generation rates (heat flow per unit time)
- constant temperature boundaries

The element adopted for the thermal analysis is the following.

PLANE 55: bidimensional element, quadrilateral (4 nodes) shaped.



It's characterized by only one DOF per node: temperature. Furthermore, a steady-state thermal analysis could be either linear, with constant material properties; or nonlinear, considering material properties that depend on temperature.

As state before, the investigation of an electrothermal problem involves both electromagnetic and thermal analysis. Because of it, the solving algorithm must have a loop structure, switching from the electromagnetic to the thermal one at every very time-step. This build is well described in the block diagram of figure 3.3.

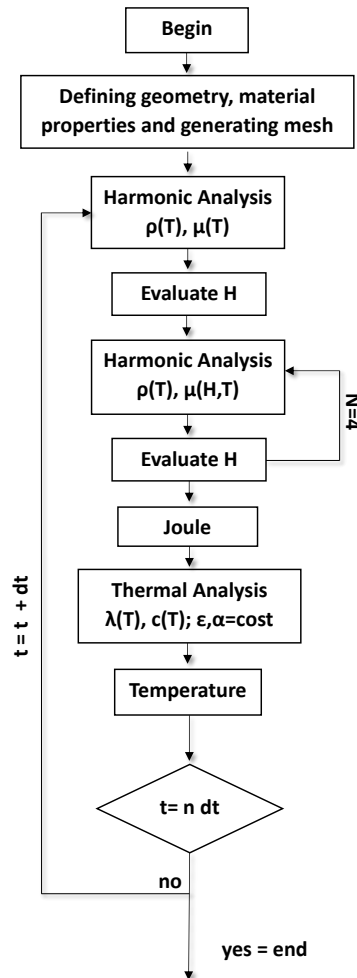


Figure 3.3: Flux diagram describing the algorithm used in Ansys APDL for solving the electromagnetic problem.

The algorithm start with a first stage in which define the geometry of the system, assign the material properties and develop and generate the mesh. After this first phase, named pre-processing (see Fig. 3.2), the electromagnetic harmonic analysis takes and reads the predefined material properties, loads the applied current (electromagnetic load) and fixes boundary conditions. Once the harmonic analysis solution has been reached, the generated heat, expressed as joule losses, is calculated from eddy currents' distribution. Since the thermal DOF is unique, the final temperature distribution within the workpiece is computed, knowing the thermal boundary conditions. The number of time-steps dt depends not only on the suited heating time but also on the desired accuracy.

3.2.1 The Preprocessing stage

In this study, the workpiece is formed of two hollow cylinders made of steel C45 (see Tab. 1.1), paired and ready to be jointed, as already presented in 1.3. The area of interest for the investigation, or rather the region surrounded the HAZ, presents the following geometrical measures:

Table 3.1: Main geometrical sizes of the interested area

length	$\ell=245$ mm
external diameter 1	$d_{1e}=232$ mm
external diameter 2	$d_{2e}=241$ mm
internal diameter	$d_i=183$ mm

To carry out a correct analysis, the time-dependent trends of the material properties have to be defined. The first two diagrams below are related to the harmonic analysis and the other ones regarding the thermal one.

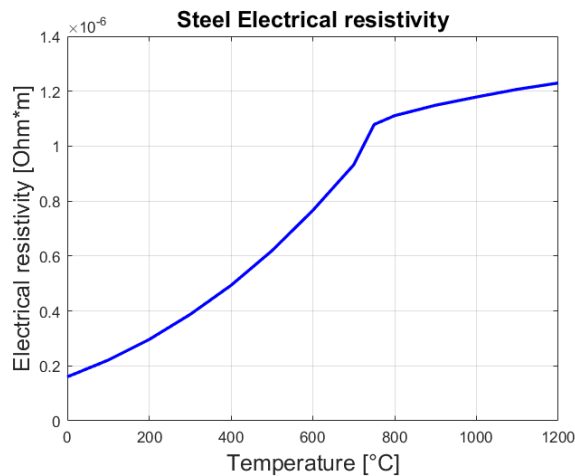
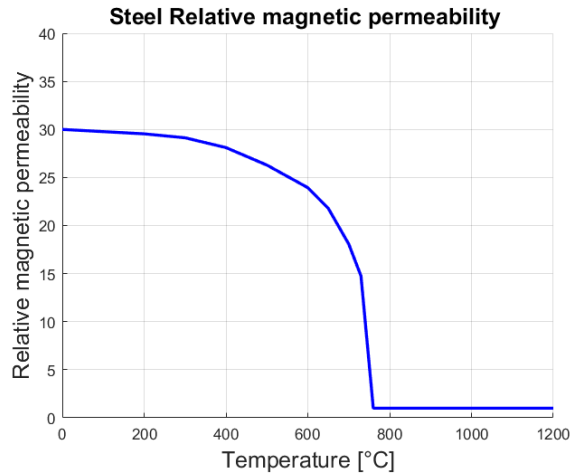
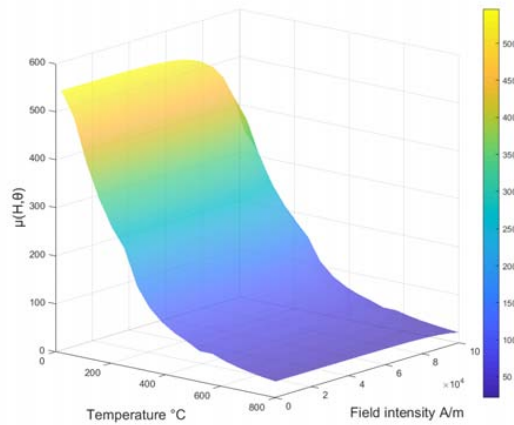


Figure 3.4: Electrical resistivity – ρ

The trend is nonlinear with the temperature. As already outlined in Sec.2.4, the electrical resistivity increase more in the range of temperature between 0 to 800 °C; whereas, it's slow down for further increasing temperature, reaching a value equal to five times the one at ambient temperature at 1200 °C.



(a) Relative magnetic permeability – $\mu(T)$



(b) Relative magnetic permeability – $\mu(H, T)$

In this study has been chosen to carry out an analysis for both the cases illustrated in the above diagrams. At first, the magnetic permeability has been considered a function of the only temperature. Later, the analysis has been run considering also the dependence with the magnetic field intensity. Although μ does not change too much in the range of temperature that characterizes a preheating process ($T_{max} \approx 300 \div 400$ °C), as will be discussed later, it results that simulations using $\mu(T, H)$ curve are more detailed and closer to the real behaviour of the workpiece. The characterisation of the surface curve of $\mu(T, H)$ has been made on the basis of a model presented in [5], here briefly presented.

Model A – The relative magnetic permeability is approximated with the formula:

$$\mu(T, H) = 1 + f(T) \cdot \mu_{20}(H) \quad (3.14)$$

where μ_{20} is the field-dependent relative permeability at room temperature, and the function $f(T)$ is evaluated by mean of the following

$$\begin{cases} f(T) = 1 - e^{\left(\frac{T-T_c}{C}\right)}, & T < T_1 \text{ with } T_1 = T_c + C \ln 0.9 \\ f(T) = e^{\left(\frac{10(T_2-T)}{C}\right)}, & T > T_1 \text{ with } T_2 = T_1 + 0.1C \ln 0.1 \end{cases}$$

where T_c the Curie temperature and C a constant.

$$B(H) = \mu_0 H + B_s \frac{H_a + 1 - \sqrt{(H_a + a)^2 - 4H_a(1 - a)}}{2(1 - a)}$$

with

$$H_a = \frac{\mu_0 H (\mu_{r_i} - 1)}{B_s} \quad \text{A/m,}$$

where μ_{r_i} is the initial relative permeability value, B_s the saturation value of the induction field and $a = 0.5$ an adjusting coefficient. The chosen values for the parameters are listed in the table below.

T_c	770 °C	μ_{r_i}	600
C	20 °C	B_s	2.05 T

Finally, calculating $\mu_{20}(H)$ as $\mu_{20}(H) = \frac{B(H)}{\mu_0 H}$ and substituting it in Eq. (3.14) one obtains the desired $\mu(H, T)$ curves.

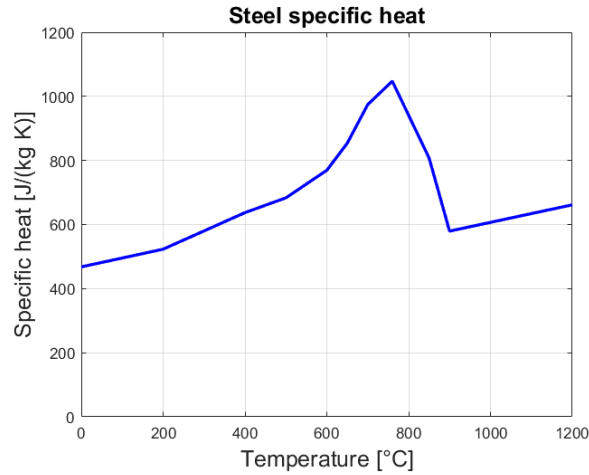


Figure 3.5: Specific heat – c

Now, the chart of Fig. 3.5 is related to the specific heat of steel C45. It can be

seen that it varies roughly linearly for temperatures below the Curie point, at which it reaches the peak value; over T_c it falls steeply before starting growing linearly again, at a lower rate.

At last, it can be shown by the thermal conductivity chart, Fig. 3.6, as the heating of the workpiece does not improve the transmission of heat. Thus, the thermal conductivity decrease till reaching a minimum at the Curie point after which starts growing linearly.

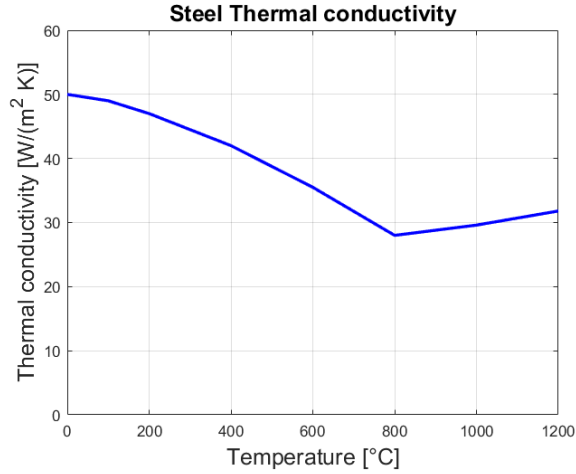


Figure 3.6: Thermal conductivity – k

The next step in the preprocessing stage is to define the mesh parameters and air-box dimensions. Firstly, recalling that the induced power concentrates on a surface layer and has an approximately exponential trend, function of the penetration depth δ , the mesh should be finer in the surface proximity. It means that, within a thickness equal to the penetration depth, there should be at least five mesh elements. At a fixed frequency therefore, δ varies with temperature as shown in Fig 3.7.

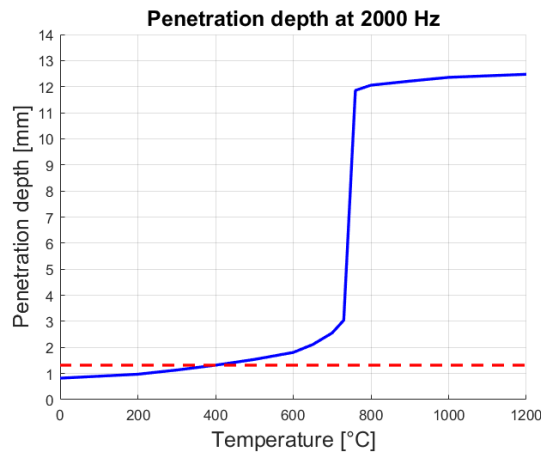


Figure 3.7: Penetration depth in function of temperature at a fixed frequency.

The diagram refers to the maximum frequency at which this investigation has been pursued, or $f = 2000$ Hz. Following these considerations, the mesh minimum size has been set to meet the constraint, considering that at the higher temperature reached in the process (about 400 °C) δ is equal to $1,37$ mm.

For what concerns the air-box, its dimensions must be much greater than the inductor-load system, whilst an excessive air-box area bears to unnecessary computational costs. Since the electromagnetic boundary conditions ($\mathbf{A} = 0$) are set at the edge of the air-box, an inadequate dimension of it gives rise of errors.

Implementation of $\mu(T, H)$ into the script

The approach pursued in this investigation consists on evaluating several $\mu - T$ curves at different magnetic field strength values. The curves obtained by the employment of the model presented in the previous paragraph are shown in Fig 3.8. The diagram has been divided in order to make them clearer.

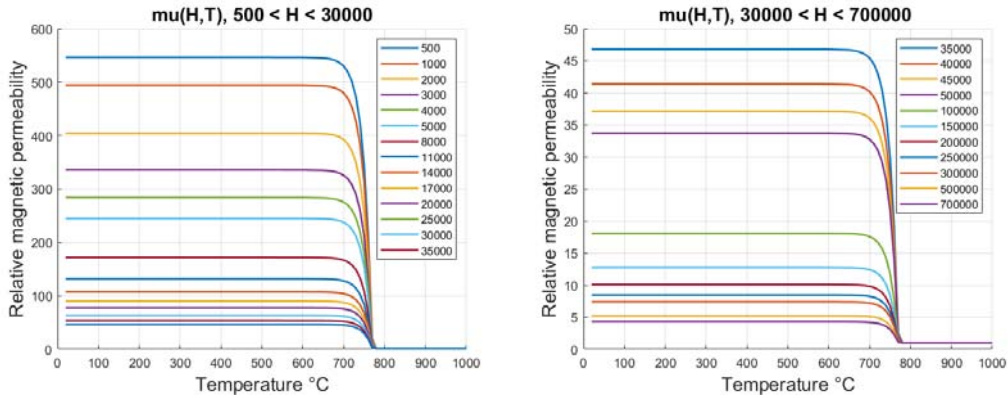


Figure 3.8: $\mu(T)$ curves obtained by implementation of *Model A* [5]

After a first computation of the electromagnetic solution, where the dependence on H of the magnetic permeability is neglected, the field strength at every element is stored in a table. Now, each element is associated with a value of the magnetic field intensity and, therefore, is possible to assign it the related $\mu - T$ curve. Consequently, a new electromagnetic solution, with the modified magnetic permeability, is calculated. This procedure has been iterated four times to reach the convergence, as shown in Fig. 3.3. The number of iteration was estimated comparing the power losses in two consecutive steps; after $N = 4$ iterations the losses remain almost constant denoting that the convergence has been reached. Although this approach increases the computational complexity of the script, it permits to obtain a more realistic simulation, taking in consideration, for instance, the higher saturation of the superficial layers in respect to deeper ones.

3.3 Strategy of investigation

The main goal of the investigation is to reach a feasible temperature within the interested zone. As already presented in 1.2, this goal temperature T_{PH} should overcome the martensite initial temperature M_s to ensure a good quality weld. Besides that, the temperature distribution must be as uniform as possible in the heat-affected zone; this region is assumed extending for twice the value of the cylinder wall thickness, on both sides of the weld bead. To meet the goal, after having built the basic geometries of the inductor-load system, the investigation has been pursued following a strategy here briefly presented.

Initially, the magnetic permeability has been considered as a function of the only temperature. Hence, a few simulations as been run to find the best inductor's parameters (i.e. the mutual distance of the active parts, inductor-load air-gap, inductor and flux concentrators thicknesses) varying the applied current and frequency at a fixed heating time t_h . The investigation continues using the values that output the best temperature distribution, to find the more suitable heating time. If modifying the time of the process, it is necessary to act again on the geometrical or electrical parameters, the investigation forms a loop that ends with the definition of the system parameters. The strategy is applied also considering the magnetic permeability dependence with the magnetic field intensity, although the parameters do not vary considerably. The analysis in these latter cases is conducted by applying a constant current in all the discretized steps. A further investigation has been carried out considering a power control, verifying if such control can improve the process in terms of heating time and energy consumption. Besides, an analysis at constant power has been done switching the attention to the costumers' side, evaluating which could be the nominal power of the system. In this final investigation, all the upstream power losses related to the power electronics and cables have been neglected.

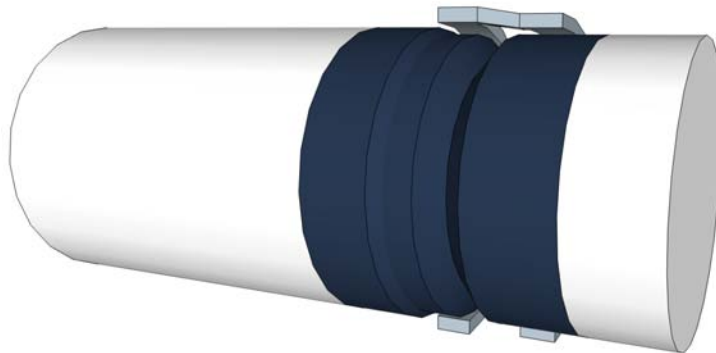


Figure 3.9: Sketch of the system with the HAZ in dark blue (not to scale).

In particular, the choice of geometrical parameters is constrained by mechanical and design reason. As shown in Fig.3.9 the workpiece presents a diameter variation within the HAZ. That brings to adopt a particular choice for what concerns the position of the C-shaped inductor. Besides, the choice of this coil design has been driven by mechanical limitations. The issue of installing a single-turn coil around the already paired cylindrical parts forming the workpiece leads to such choice. On the contrary, the selection of electrical parameters, current and frequency, has more degrees of freedom.

3.3.1 Parameters determination

Frequency

The evaluation of the proper frequency value takes into consideration several aspects. First of all the kind of heating treatment that has to be conducted. Moreover, the frequency is chosen considering the wall thickness of the body to be heated to meet the goal of temperature uniformity. Besides, the value of m should be chosen higher than $2 \div 2.5$ to don't affect the efficiency of the system, recalling that m relates the load's diameter with the penetration depth, then the applied frequency. Although a high value of m leads to good electrical efficiency, it generates a superficial power distribution increasing thermal losses and heating time. Hence, for different diameters exists a range of optimal frequency that permits to obtain the target temperature distribution without lessening too much the efficiency. Summarizing:

- if $m < 2$ the electrical efficiency is low;
- if $m = 2.5$ the efficiency excellent;
- if $2 \leq m \leq 5$ the process is characterized by a sufficient efficiency;
- if $m \geq 7$ the thermal efficiency falls.

For assuring an optimal system efficiency, the frequency value has to be determined considering $m = 2.5$ as follow:

$$m_{hot} = \frac{\sqrt{2}r_e}{\delta} = \sqrt{2\pi \frac{\mu\mu_0}{\rho}} \sqrt{f} r_e = 2.5$$

with δ evaluated with the characteristics of the "hot" material ($\approx 400^\circ\text{C}$). Thus, solving the previous equation for f gives a frequency value of ≈ 1 Hz. Adopting this value would lead to long heating time, although it maximizes the overall efficiency. For this reason, the frequency value has been chosen to optimize the heating time, keeping as large as possible the penetration depth.

As shown by Fig. 2.14, the adoption of a relatively low frequency (*curve* f_1), yields to H roughly constant over the whole thickness of the tube while G varies

linearly. Hence, for the analysis at constant power, frequency is set to $f = 650$ Hz corresponding to $m \approx 63$. Will be highlighted, however, that introducing a power control the adoption of higher frequency values yields to better results.

Air gap between inductor and workpiece

The load has to be coupled in the best way with the inductor. Reducing the air gap leads to an increase in the efficiency and power factor ($\cos \varphi$). Conversely, the gap should not be too thin to avoid strong radiation caused by the hot body which would overheat the inductor. As already highlighted, the region of interest presents a diameter variation and, therefore, the inductor's active parts have been set at different distances from the workpiece. The following table shows some recommendation for the choice of the air gap:

Frequency [kHz]	Air gap [mm]
1 – 3	3 – 6
10 – 25	2 – 3.8
50 – 450	1.5 – 2.25

Being the frequency equal to 650 Hz in the constant power case but higher in the other analyzed ones, the air gap should be set approximately equal to 5 mm. Further considerations have been made concerning mechanical constraints; the gap should have a value that does not imply installation issues seeing the complex geometry of both inductor and load. Besides, as shown in Fig. 3.9, the gap underneath one active part is not constant. Then the air gap presents two different values: equal to 4,5 mm for the active part facing the diameter variation and equal to 5 mm on the other part, both referring to the larger diameter.

Inductor design

The copper made inductor geometry is strictly related to the aforementioned mechanical constraints mainly imposed by the load geometry. Being the workpiece composed of two cylindrical parts paired to be welded the choice of an open, C-shaped, inductor has been driven both by these mechanical reasons and by requirements advanced by the industrial customer who proposed this study. Besides, the inductor has been designed with rectangular cross-section embedding a water cooling channel, as shown in Fig. 3.11. The active parts are covered by a U-shaped magnetic flux concentrators; they improve the efficiency of the process partly by improving the electromagnetic coupling between the workpiece surface and the active parts of the inductor, as well as by reducing stray losses [11]. In general, appreciable

improvements in electrical efficiency can be achieved when flux concentrators are applied to particular inductor geometries.

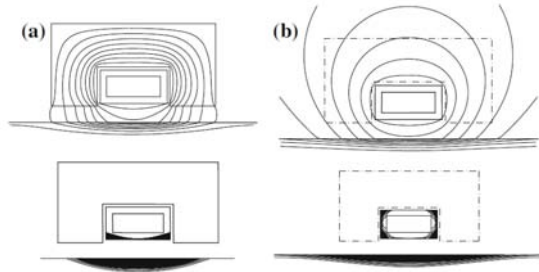


Figure 3.10: Distributions of field lines and induced power with (a) and without (b) flux concentrator [3].

The thickness of the inductor must fulfil a condition expressed by the following:

$$s \geq \frac{\pi}{2} \delta_{coil} ;$$

then adopting a thickness greater than a certain value avoids that the inductor losses increase dramatically. This boundary value is evaluated considering δ_{coil} the penetration depth of the inductor, assuming constant and equal to $\rho_{coil} = 1.9 \cdot 10^{-8} \Omega \text{ m}$ the copper electrical resistivity, being the inductor water-cooled. It results to be $s \geq 4.3 \text{ mm}$ for $f = 650 \text{ Hz}$ and $s \geq 2.4 \text{ mm}$ for $f = 650 \text{ Hz}$; thus the thickness has been chosen equal to 3 mm although it doesn't fulfil the requirement at lower frequency. The choice will be justified later with the discussion of the investigation results.

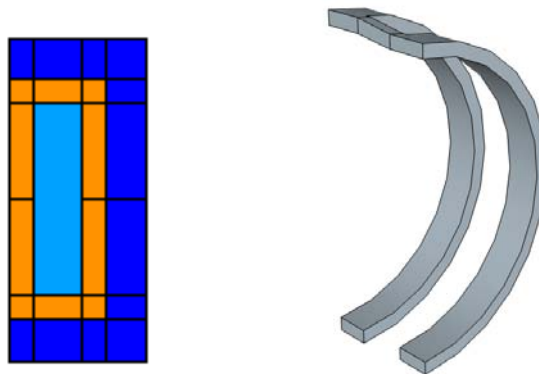


Figure 3.11: On the left the inductor cross-section (*coil in orange, water channel in light blue and flux concentrator in blue*); on the right an overview of the inductor (not to scale).

The following table summarized the cross section dimensions adopted in the investigation.

Table 3.2: Coil cross-section geometrical parameters

Coil thickness s	3 mm
Longer side B	30 mm
Shorter side A	12 mm
Flux concentrator thickness ϕ	5 mm

3.4 Case study 1

Several analysis has been pursued to reach the investigation goal, employing the strategy presented in 3.3. In Fig. 3.12 is possible to see the inductor active parts.

1

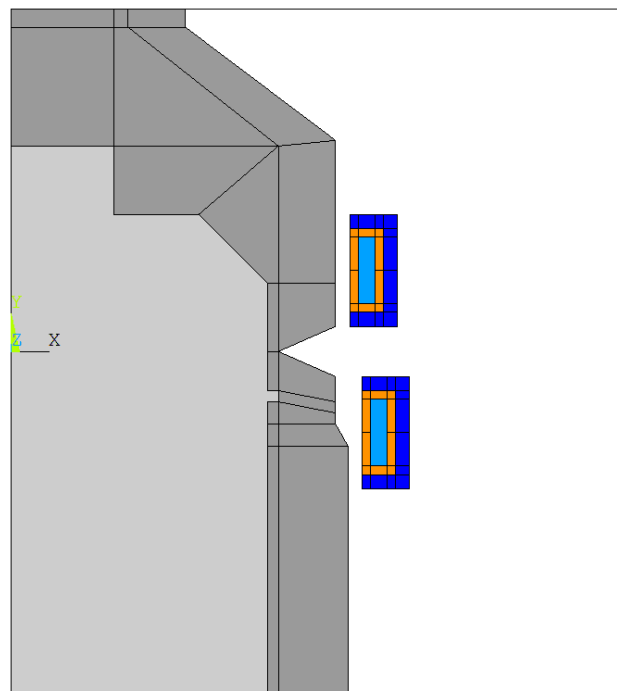
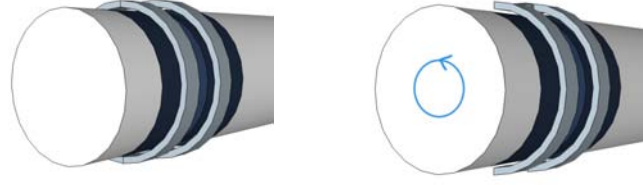


Figure 3.12: Geometry of the system

Since the model differs from the real system, (see Fig. 3.13) the applied current in the model results $\sqrt{2}$ times smaller of the real one. Referring to the conservation of the energy, in order to obtain the same induced power evaluated in the simulation, the real inductor has to carry more current and keeps in rotation.



(a) Sketch of the 2D model (not to scale) (b) Sketch of the real system (not to scale)

Figure 3.13: Difference between simulated and real system

$$Q_{2D} = Q_{real} \quad \text{follows that} \quad P_{real} = 2 P_{2D}$$

and, being the active power proportional to I^2 (with I rms value) it results:

$$I_{real}^2 = 2 I_{2D}^2 \quad \text{or} \quad I_{real} = \sqrt{2} I_{2D}.$$

However, the simulations have been done neglecting this fact and this correction made at the end.

The input parameters adopted in this first analysis are listed in the table below.

Geometrical parameters	
Coil thickness s	3 mm
Longer side B	30 mm
Shorter side A	12 mm
Flux concentrator thickness ϕ	5 mm
Active parts mutual distance	29 mm
Air-gap active part 1 (above)	5 mm
Air-gap active part 2 (below) ²	4.5 mm
Electrical parameters	
Current	3300 A
Frequency	650 Hz

This simulation was pursued maintaining the current constant throughout all the time-steps and considering the magnetic permeability a function of the only temperature. A relatively high value of 3300 A is adopted in order to limit the heating time and generally the energy consumption too. The heating process was declared finished when the temperature in the inner layer of the tube wall reaches $\approx 300^\circ\text{C}$.

²Both the active parts' air-gaps refer to $d_{1e} = 232\text{mm}$

Electrical results:

Heating time	300 s
Energy	1.44 kW h
Maximum voltage	17.28 V

The energy is calculated considering both the induced energy in the workpiece and the inductor losses. The APDL command *POWERH* returns directly the sum of the induced power and inductor power losses.

Thermal results

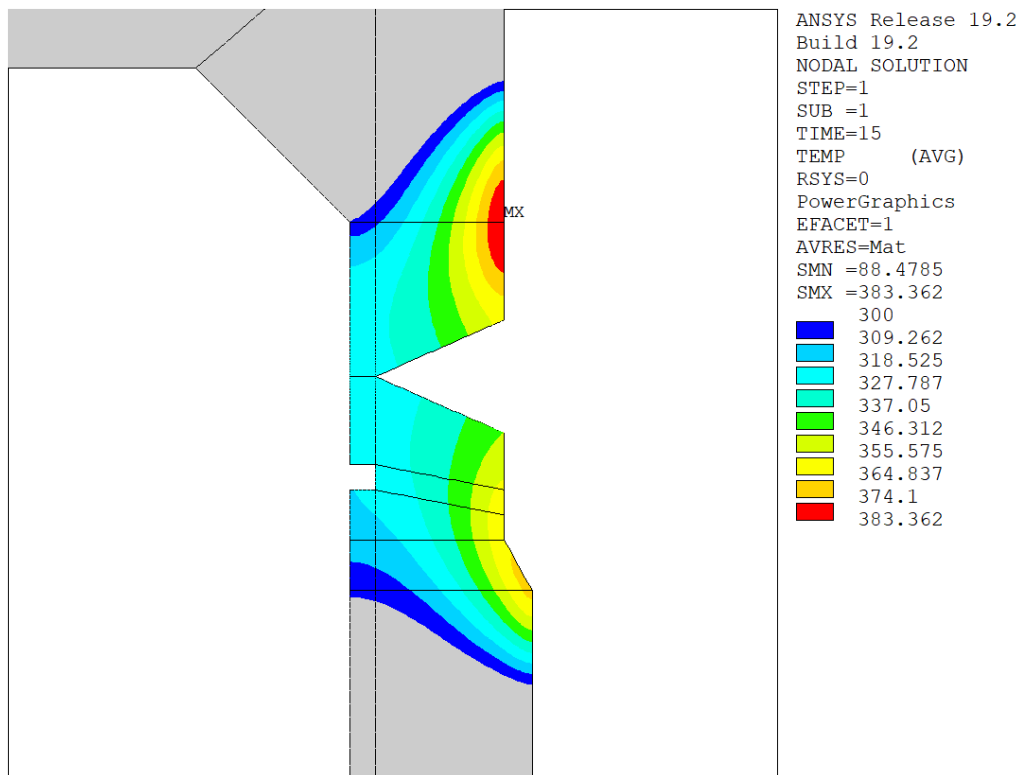


Figure 3.14: Case 1 contour plot of the final temperature distribution zoomed in the region of interest

On the side of the contour plot shown in Fig. 3.14 is present a legend showing the different temperature values. Notice that, in the upper side of the HAZ there's a hot zone, caused by the thinner air gap between the load and the upper active part of the inductor. The choice of differing the air gap of the active parts was adopted, therefore, to avoid the arising of hot-point in the region of the diameter variation, region interested in higher stresses.

The temperature distribution obtained by this simulation fulfil the requirements

although a few consideration can be made. First, the long heating time is a consequence of both the considerable wall thickness and of the current value adopted. Besides, it has been chosen to hold the applied current value under a maximum of $4 \div 5$ kA to limit the temperature stresses on the inductor active parts, considering also the correction factor between real and simulated cases.

3.5 Case study 2

This analysis was carried out to check the effective necessity of considering the double dependence of magnetic permeability $\mu(T, H)$. Then, a first simulation was done adopting the same geometrical and electrical parameters of the Case study 1.

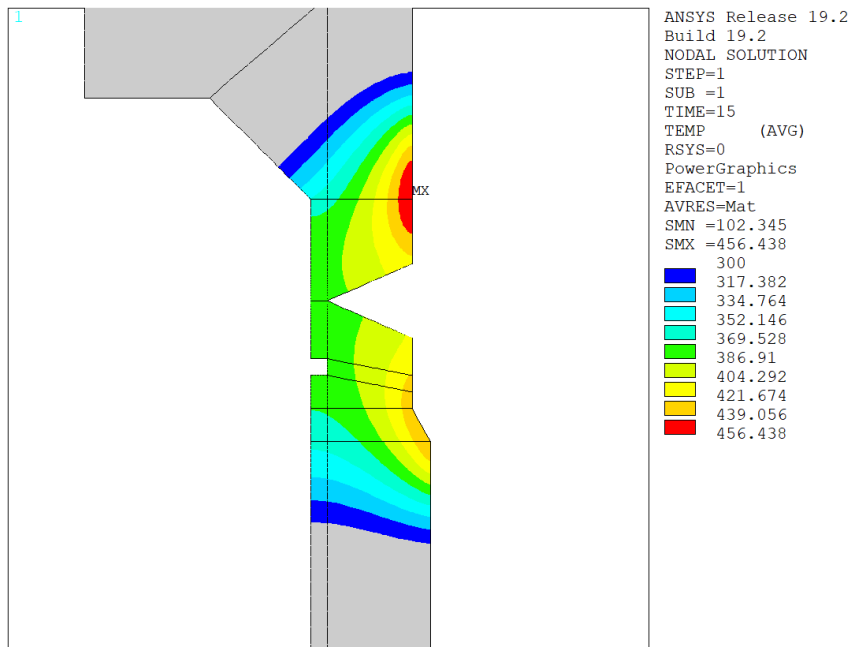


Figure 3.15: Contour plot of case 1 analysis considering $\mu(T, H)$

As shown in Fig. 3.15, the effect of considering also the magnetic field dependency of μ is marked; it results in higher temperature with same heating time and current. By that, the higher saturation of superficial layers have been taken into account.

Hence, new electrical parameters was employed and a new simulation carried, as follows:

Electrical parameters	
Current	3000 A
Frequency	650 Hz

Electrical results:

Heating time	300 s
Energy	1.38 kW h
Maximum voltage	17.52 V

As outlined by the above table, the employment of $\mu(T, H)$ permits to reduce the applied current value while the energy and maximum voltage values remain close to the previous ones.

Thermal results

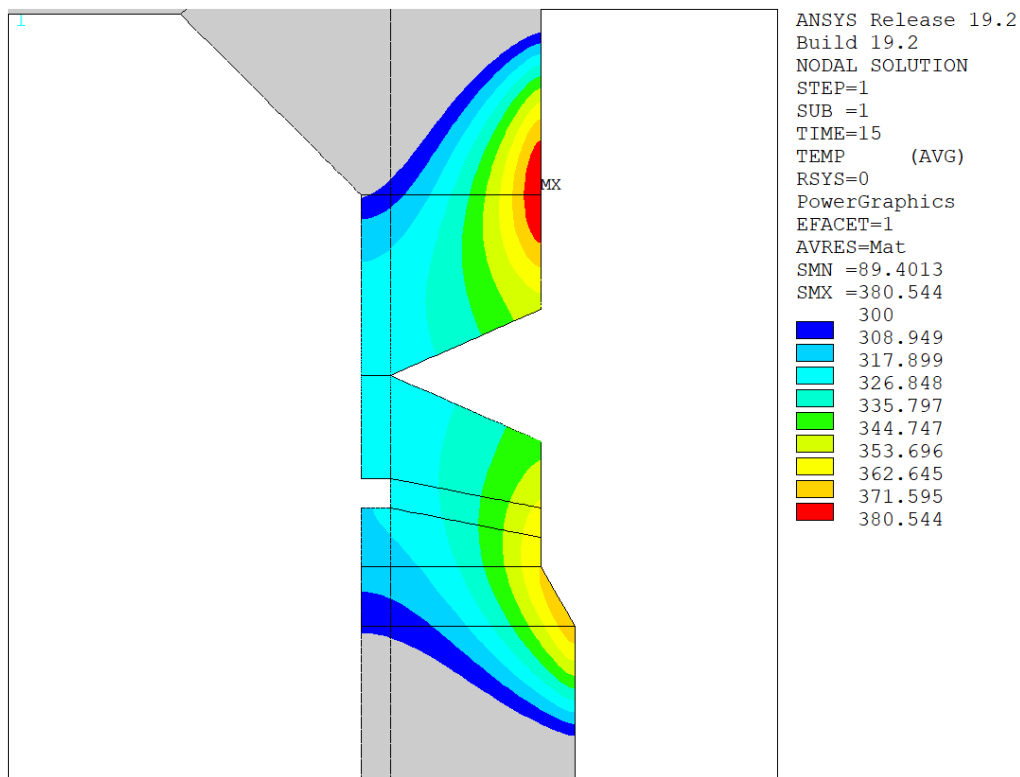


Figure 3.16: Case 2 contour plot of the final temperature distribution zoomed in the region of interest

Figure 3.16 shows that, as in the first analysis, the temperature distribution fulfil the investigation requirements presenting a good uniformity within the entire wall thickness. Besides, it presents again a hot spot in generated by the same reasons aforementioned. In respect with the first analysis, it's important to point out, although an increase of computational cost, the adoption of a more realistic material behaviour yields concrete and different results.

3.6 Case study 3

The investigation continues with a further analysis aiming to reduce the process parameters and in particular the heating time. Material properties remain the same adopted in the previous analysis. In order to improve the performances of an induction heating system and reducing the heating time while providing the required temperature uniformity, power pulsing can be applied [12]. It refers to a technique that applies bursts of power to maintain the target surface temperature in order to obtain the desired temperature distribution within the thickness. Pulse heating is characterized by a series of "heat on" and "heat off" cycles until the required uniformity is obtained.

Adopting this kind of power control, heating cycles parameters was evaluated in order to not overcome a surface temperature of 430 °C. Referring to the current-time chart below, the time parameters are:

Time ON1 - t_1	140 s
Time OFF1 - t_2	143 s
Time ON2 - t_3	153 s
Time OFF2 - t_f	156 s

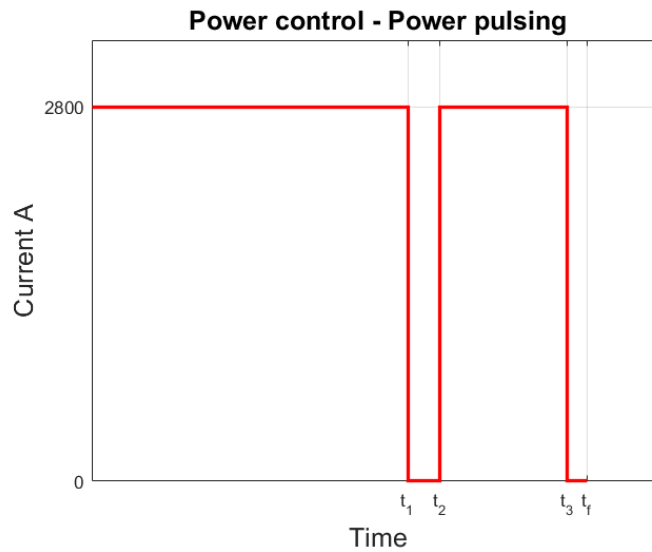


Figure 3.17: Power pulsing

Hence, four heating cycles was defined: a first "heat on" of 140 s followed by a "heat off" 3 s long and a further "heat on" of 10 s ending with a "heat off" with the same time of the first one. The bursts of power ended when the surface temperature reaches nearly the maximum allowed value. The electrical parameters adopted in this analysis are:

Electrical parameters	
Current	2800 A
Frequency	1200 Hz

Notice that, a higher value of frequency is applied to reach faster the target surface temperature then exploiting the thermal diffusion toward the core during the heat-off time. Besides, the applied current is lower.

Electrical results:

Heating time	156 s
Energy	1.11 kW h
Maximum voltage	26.91 V

Comparing with the electrical results gained in Case 1 and Case 2, it should be noticed a marked reduction of time as well as a decreasing of energy consumption.

Thermal results

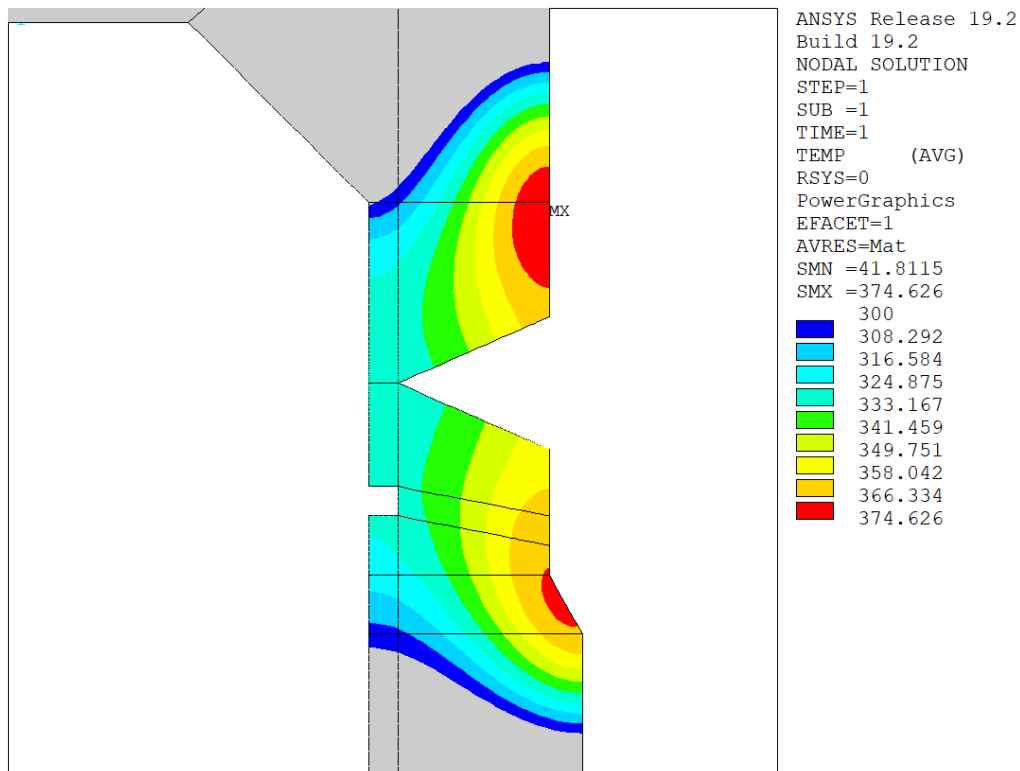


Figure 3.18: Case 3 contour plot of the final temperature distribution zoomed in the region of interest

Figure 3.18 highlights that employing the power pulsing technique the final temperature distribution is even more uniform than in the previous cases. Although it gives rise of a hot spot in the diameter change zone, the air gap corresponding to the bottom active part was reduced to 3.6 mm. It allows, however, to gain a deeper and more homogenous temperature distribution in the lower region of the HAZ in respect to the first two cases.

3.7 Case study 4

The heating time can be reduced even more adopting the accelerated heating approach [12]. It employs an exponential reduction of the current value next the achievement of a satisfy surface temperature. Apparently, in order to provide this heating technique it's necessary to have a power supply that allows a progressive reduction of the output power. Besides, it permits to lessening thermal stresses caused by elevated temperature gradients, affecting in particular high carbon steels.

Parameters characterizing the exponential decay are listed in the following table, while Fig. 3.19 illustrates the current time profile used in this method.

Time ON1 - t_1	120 s
Time EXP - t_f	25 s

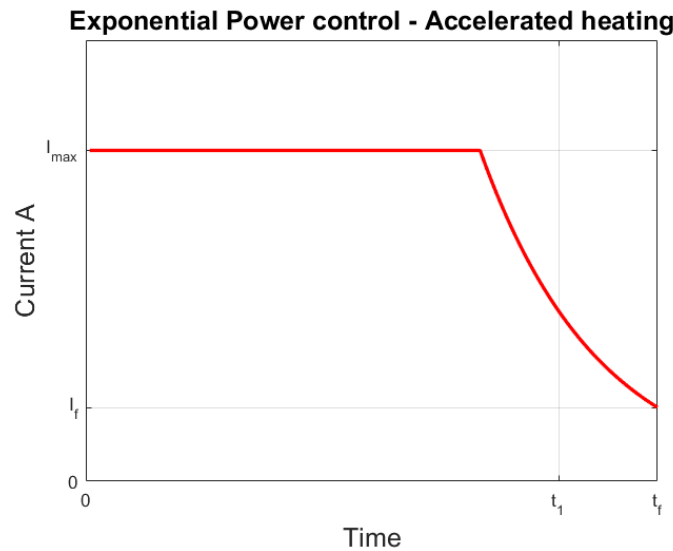


Figure 3.19: Accelerated heating

The current's exponential decay $I(t) = I_{max} e^{t/\tau}$ is characterized by a *time constant* τ of 70 s. Furthermore, the same material features, as well as the same geometrical configuration of Case 3, are adopted in this analysis whereas, new electrical parame-

ters are selected as listed below.

Electrical parameters	
Maximum current - I_{max}	2250 A
Final current - I_f	1612.2 A
Frequency	2000 Hz

The value of frequency is higher than in the analysis adopting the pulsing power approach. Selecting this frequency value allows reaching faster a suitable surface temperature which does not exceed even 410 °C.

Electrical results:

Heating time	145 s
Energy	1.03 kW h
Maximum voltage	32.96 V

Employing the accelerated heating, therefore, brings to a further decrease of the heating time as well as a reduction of energy consumption.

Thermal results

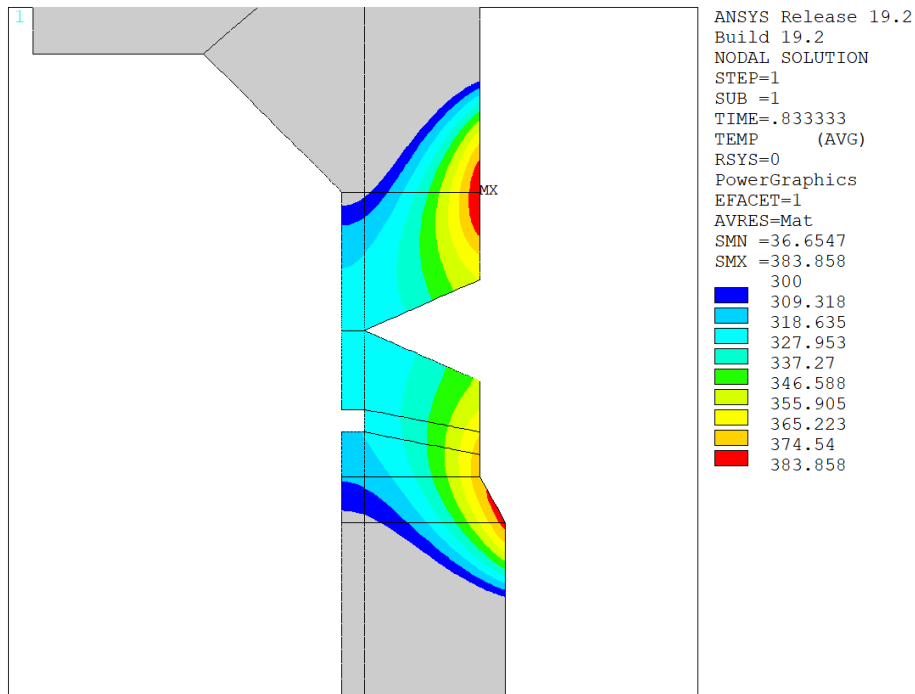


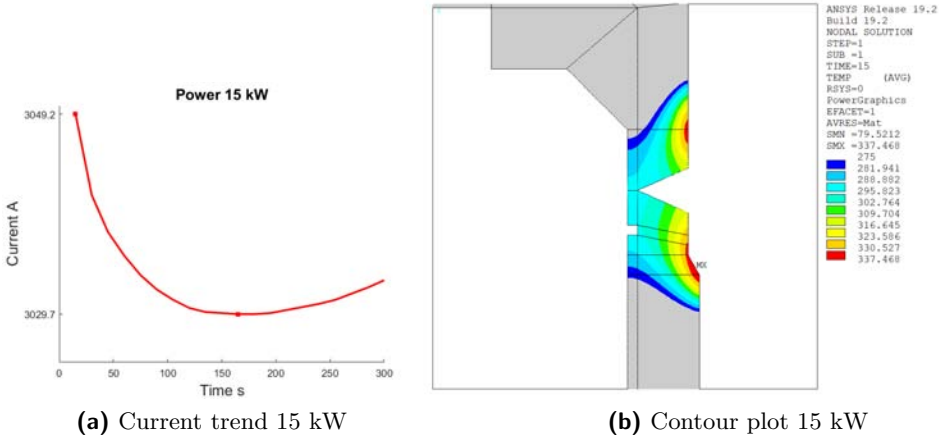
Figure 3.20: Case 4 contour plot of the final temperature distribution zoomed in the region of interest

Figure 3.20 shows how, by applying this power control, is possible to reduce the lower hot zone in respect to the previous simulation case. The temperature distribution fulfils, therefore, the study requirements denoting a good homogeneity throughout the wall thickness. On the contrary, it presents a lower temperature on the inner layer of the wall at the edge of the region of interest. Thus, employing this technique results in a worthwhile temperature distribution as well as the lowest energy consumption and heating time overall. Besides, a double exponential cycle could be implemented to obtain a finer temperature homogeneity lessening, even more, the thermal stresses. However, in order to keep the simulation model as simple as possible, limiting the operational costs, in this study, this approach was not implemented.

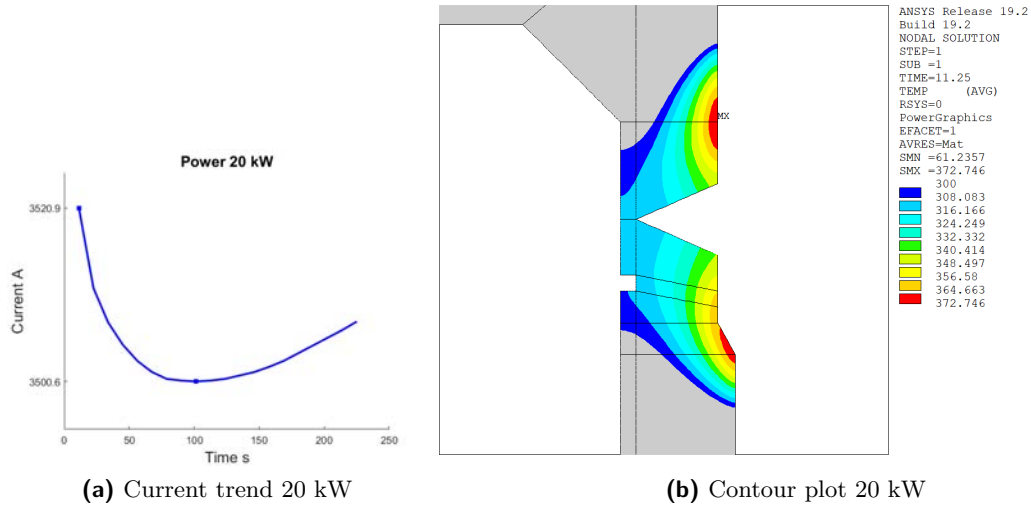
3.8 Case study 5

This study case was analysed to evaluate which should be the generator power that fulfils the temperature distribution requirement for a preheating process, or rather with the aim of study the problem from the customer point of view. Three cases with different induced power are analysed: a first with $P = 15\text{kW}$ then a second with $P = 20\text{kW}$ and the last one with $P = 30\text{kW}$. The solver algorithm was modified to keep the power constant throughout the entire heating time whereas the applied current and voltage vary. Besides, the magnetic field dependence of μ was neglected to keep the model as simple as possible and avoiding excessive operational costs. The geometry of the system is equal to the one used in the first case study and the frequency selected equal to $f = 650\text{Hz}$ since any power control wasn't implemented.

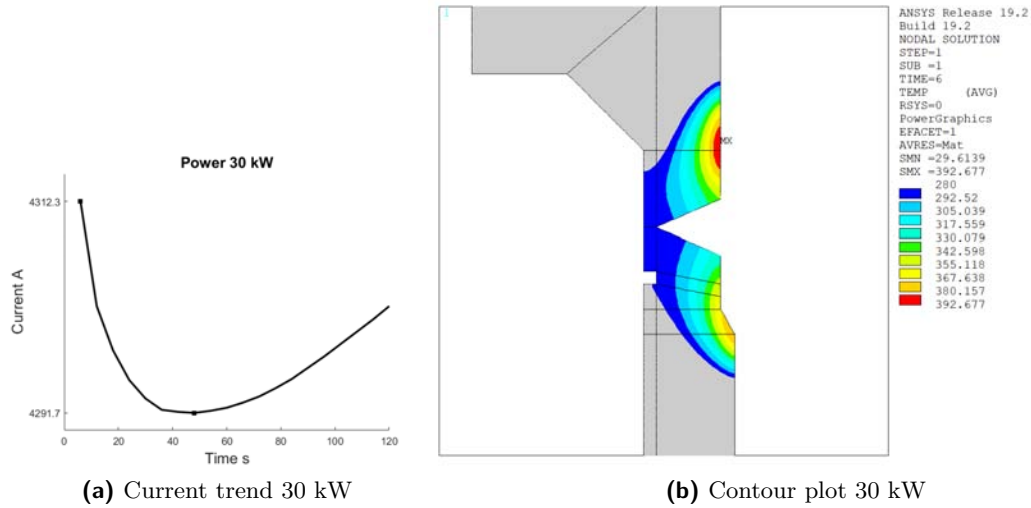
Inductor-load power – 15 kW



Inductor-load power – 20 kW



Inductor-load power – 30 kW



Process parameter	15 kW	20 kW	30 kW
Maximum current	3049.2 A	3520.9 A	4312.3 A
Heating time	300 s	225 s	120 s

It should be paid attention that the results refer to the active power involved in the system or rather the sum of induced power and inductor losses. Hence, for evaluate the suitable generator nominal power the efficiency of upstream components must be taken into account. The best result is achieved for a system power of 20kW. As

shown by its contour plot, a good temperature distribution is achieved in a relatively short heating time (225 s). Notice that the current presents the same behaviour for every analysed case since it depends by the material properties' trend with temperature. At first, the current decreases due to the resistivity growth that ease the rising of temperature. After reaching a minimum, it grows smoothly because of the more accentuated effect of magnetic permeability at higher temperature in respect with the resistivity one. It should be noticed, however, that the current value doesn't oscillate substantially although it varies more for higher power.

Chapter 4

Summary of results

This study, carried out at ETP the Hannover Institute of Electrotechnology, has the main goal to investigate and show the possibility of adopting an induction heating system to provide the preheat treatment on a thick tubular workpiece before welding it. The numerical approach permits to simulate with accuracy the temperature distribution and to study a complex geometry with a 2D model due to axial symmetry. The application of induction heating for this particular treatment avoids, therefore, the employment of open flames reducing safety hazardous and among all cutting the risks of delayed cracking. Although induction heating systems present a higher installation cost than the open flame solution, it leads to good and controlled temperature profiles.

Throughout the study, starting from a constant power method, power controls have been implemented leading to better results, in terms of temperature distribution and energy consumption, then heating time. Specific literature proposes two power controls approaches which can improve mass heating performances; the power pulsing (case study 3) and the accelerated heating (case study 4) methods has, thus, been implemented in the numerical model. In the table below, the most significant results are presented.

	f [Hz]	t_h [s]	I_{2D} [A]	I_{real} [A]	E [kW h]	E_{saving} [%]
Case 2	650	300	3000	4242.6	1.3814	-
Case 3	1200	156	2800	3959.8	1.1126	19.46
Case 4	2000	145	2250	3182.0	1.0298	25.45

Results highlight the effective reduction of energy consumption. When applying the accelerated heating turns out the best results with an energy saving of 25.45%. It should be noticed that, as already mentioned in 3.4, the effective value of current result $\sqrt{2}$ times higher than the value applied in the simulations, consequence of the

reduction of the real model into a 2D one. Carrying practical activities would be very useful to validate the results and optimize the system parameters. Unfortunately, it was not possible pursuing them due to a lack of information from the firm who commissioned the study to ETP.

Using induction for preheating purposes before welding is still relegated to small industrial applications, especially integrated with a laser beam welding technique. The European Union, however, funded a project (*INDUCWELD*) focused on the improvement of the welding process for high strength steels by integrating induction-based heat treatment into the welding process [13].

Acknowledgements

I would love to thank my supervisor Pf. Dr. - Ing. Egbert Baake and Dr. Ing. Alexander Nikanorov. First, Pf. Baake for giving me the possibility of carrying my master thesis work at ETP and for his professional and moral support. Then, Ing. Nikanorov who guided me throughout my project daily with his technical expertise. The time spent in ETP would not be the same without the presence and help of the whole staff of the institute. In particular, I would like to thank Marco Baldan and Martin Schulze for their moral and technical support.

A thank, in particular, goes to Ing. Forzan for his support and for his commitment to keeping the exchange program between Padua and Hannover possible.

The greatest thanks go to my family who always supports me morally and economically throughout my university path. Additionally, thank you to all my friends with whom I share a bunch of beautiful moments and to LEDS (L'Energia Degli Studenti) the student association which enlightened my university life. Finally, a special thank goes to my beloved Maddalena who supports me whatever happens.

List of Figures

1.1	Cross-section of a welded butt joint	1
1.2	TTT Diagram of C45	3
1.3	Sketches of the system	4
2.1	Typical arrangement of an induction coil	6
2.2	Skin effect	7
2.3	Proximity effect [4]	7
2.4	Examples of different induction coil-load systems (a coil b load) [3].	9
2.5	Main elements of an iduction heating installation	9
2.6	Cylindrical inductor-load system	10
2.7	Bessel functions	12
2.8	Distribution of magnetic field intensity H along the radius	13
2.9	Values of the coefficients P and Q . [3]	15
2.10	Distribution of current density G along the radius	16
2.11	Influence of frequency on the induced current density	17
2.12	Distribution of specific power along the radius	18
2.13	Hollow cylinder	21
2.14	Magnetic field intensity and current density relative distributions in tubes	23
2.15	Power coefficients for hollow loads heated with an external inductor	24
2.16	Schematization of the inductor coil for calculation of its own resistance	25
2.17	Active and reactive power coefficients in tubes with internal exciting magnetic field [3]	27
2.18	Electrical efficiency of the inductor-load system	28
2.19	Quality and Power factors as a function of m	29
	(a) Ideal quality factor Q'_0 for non-magnetic materials	29
	(b) Power factor for non-magnetic material and ideal inductor-load system	29
2.20	Radial linear temperature distribution	33
2.21	Correction factor without and with surface thermal losses	34

(a)	Values of a) $F(m)$, b) $F'(m)$ and c) $F''(m)$	34
(b)	Correction factor including surface thermal losses	34
2.22	Thermal transient in uniform heating of non-magnetic workpieces . .	36
2.23	Resistivity variation of different steels (1 Inox 18 Cr Ni8; 2 Rapid steel; Carbon steel 0.06 %) [3]	38
2.24	Relative magnetic permeability depending on temperature and mag- netic field intensity	39
(a)	Values for <i>steel C45</i> [5]	39
(b)	Surface plot showing values for <i>steel C45</i> , evaluated by a model presented in [5]	39
2.25	Schematization of the heating transient of a magnetic billet, for the evaluation of heating time [3]	40
2.26	Relative variation of specific power with temperature in the case of heating a magnetic steel [3]	41
2.27	Distribution of μ within a magnetic load due to local field intensity (ρ =cost; x =distance from the surface; H_e in A/cm [3]	41
2.28	Qualitative current density distribution at Curie transition with ref- erence to the surface value (1 non-magnetic; 2 magnetic) [3]	42
3.1	Axisymmetric body example [7]	49
3.2	Flux diagram of pre-processing	50
3.3	Flux diagram describing the algorithm used in Ansys APDL for solving the electromagnetic problem.	53
3.4	Electrical resistivity – ρ	54
(a)	Relative magnetic permeability – $\mu(T)$	55
(b)	Relative magnetic permeability – $\mu(H, T)$	55
3.5	Specific heat – c	56
3.6	Thermal conductivity – k	57
3.7	Penetration depth in function of temperature at a fixed frequency. .	57
3.8	$\mu(T)$ curves obtained by implementation of <i>Model A</i> [5]	58
3.9	Sketch of the system with the HAZ in dark blue (not to scale). . . .	59
3.10	Distributions of field lines and induced power with (a) and without (b) flux concentrator [3].	62
3.11	Inductor sketches	62
3.12	Geometry of the system	63
3.13	Difference between simulated and real system	64
(a)	Sketch of the 2D model (not to scale)	64
(b)	Sketch of the real system (not to scale)	64

3.14	Case 1 contour plot of the final temperature distribution zoomed in the region of interest	65
3.15	Contour plot of case 1 analysis considering $\mu(T, H)$	66
3.16	Case 2 contour plot of the final temperature distribution zoomed in the region of interest	67
3.17	Power pulsing	68
3.18	Case 3 contour plot of the final temperature distribution zoomed in the region of interest	69
3.19	Accelerated heating	70
3.20	Case 4 contour plot of the final temperature distribution zoomed in the region of interest	71
	(a) Current trend 15 kW	72
	(b) Contour plot 15 kW	72
	(a) Current trend 20 kW	73
	(b) Contour plot 20 kW	73
	(a) Current trend 30 kW	73
	(b) Contour plot 30 kW	73

Bibliography

- [1] C. L. Jenney and A. O'Brien, *Welding Handbook, Volume 1 - Welding Science and Technology (9th Edition)*. American Welding Society (AWS), 2012.
- [2] I. Magnabosco, P. Ferro, A. Tiziani, and F. Bonollo, "Induction heat treatment of a iso c45 steel bar: Experimental and numerical analysis," *Computational materials science*, vol. 35, no. 2, pp. 98–106, 2006.
- [3] S. Lupi, *Fundamentals of Electroheat*. Springer, 2017.
- [4] S. Lupi, M. Forzan, and A. Aliferov, *Induction and direct resistance heating*. Springer, 2015.
- [5] P. Di Barba, M. E. Mognaschi, D. Lowther, F. Dughiero, M. Forzan, S. Lupi, and E. Sieni, "A benchmark problem of induction heating analysis," *International Journal of Applied Electromagnetics and Mechanics*, vol. 53, no. S1, pp. S139–S149, 2017.
- [6] L. Perumal and D. T. T. Mon, "Finite elements for engineering analysis: a brief review," in *Proceedings of the International Conference on Modeling, Simulation and Control (IPCSIT'11)*, vol. 10, 2011.
- [7] R. Bargallo, "Finite elements for electrical engineering, universitat politècnica de catalunya," *Electrical Engineering Department*, 2006.
- [8] D. N. Arnold, "Stability, consistency, and convergence of numerical discretizations," *Encyclopedia of Applied and Computational Mathematics*, pp. 1358–1364, 2015.
- [9] ANSYS.Inc, *ANSYS Mechanical APDL Low-Frequency Electromagnetic Analysis Guide*, November 2013.
- [10] ANSYS.Inc, *Thermal Analysis Guide*, April 2009.
- [11] S. Hashmi, *Comprehensive materials processing*. Newnes, 2014.

- [12] V. Rudnev, D. Loveless, and R. L. Cook, *Handbook of induction heating*. CRC press, 2017.
- [13] J. Stein and P. Kallage, “Induction assisted welding technologies in steel utilization–inducweld,” tech. rep., RFSR-CT-2005-00040, Res. Prog. Fund for Coal and Steel, 2010.